

E201 743

2

PL-TR-93-2112

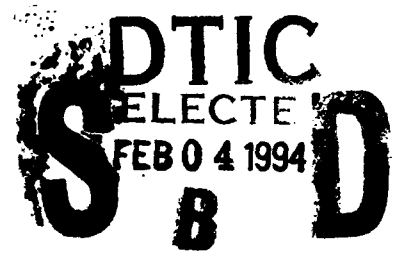
AD-A275 570



# ACTIVE ELECTRON AND ION BEAM EXPERIMENTS IN SPACE

M. Ashour-Abdalla  
P.L. Pritchett  
D. Schriver

University of California  
Institute of Geophysics and Planetary Physics  
405 Hilgard Avenue  
Los Angeles, CA 90024



February 1993

Final Report  
18 February 1988 - 31 December 1992

Approved for public release; distribution unlimited



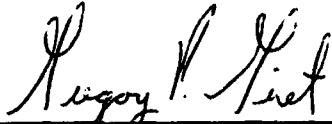
**PHILLIPS LABORATORY**  
Directorate of Geophysics  
**AIR FORCE MATERIEL COMMAND**  
HANSCOM AIR FORCE BASE, MA 01731-3010

4986 94-03943



94 2 03 160

**"This technical report has been reviewed and is approved for publication"**



---

**GREGORY P. GINET**  
Contract Manager  
Plasmas & Fields Branch  
Space Physics Division



---

**NELSON C. MAYNARD**  
Branch Chief  
Plasmas & Fields Branch  
Space Physics Division



---

**RITA C. SAGALYN, Director**  
Space Physics Division

***This report has been reviewed by the ESC Public Affairs Office (PA) and is releasable to the National Technical Information Service (NTIS).***

***Qualified requestors may obtain additional copies from the Defense Technical Information Center. All others should apply to the National Technical Information Service.***

***If your address has changed, or if you wish to be removed from the mailing list, or if the addressee is no longer employed by your organization, please notify PL/TSI, Hanscom AFB, MA 01731-3010. This will assist us in maintaining a current mailing list.***

***Do not return copies of this report unless contractual obligations or notices on a specific document requires that it be returned.***

REPORT DOCUMENTATION PAGE			Form Approved OAS No. 0704-0100	
<small>Public reporting burden for this collection of information is estimated to average 1 hour per response, including the time for reviewing instructions, searching existing data sources, gathering and maintaining the data needed, and completing and reviewing the collection of information. Send comments regarding this burden estimate or any other aspect of this collection of information, including suggestions for reducing this burden, to Washington Headquarters Service, Directorate for Information Operations and Reports, 1215 Jefferson Davis Highway, Suite 1204, Arlington, VA 22202-4302, and to the Office of Management and Budget, Paperwork Reduction Project (0704-0100), Washington, DC 20503.</small>				
1. AGENCY USE ONLY (Leave blank)	2. REPORT DATE February 1993	3. REPORT TYPE AND DATES COVERED Final (18 Feb 1988-31 Dec 1992)		
4. TITLE AND SUBTITLE Active Electron and Ion Beam Experiments in Space		5. FUNDING NUMBERS PE 61102F PR 2311 TA G6 WU AA  Contract F19826-88-K-0011		
6. AUTHOR(S) M. Ashour-Abdalla P.L. Pritchett D. Schriver		7. PERFORMING ORGANIZATION NAME(S) AND ADDRESS(ES) University of California, Los Angeles Institute of Geophysics and Planetary Physics 405 Hilgard Avenue Los Angeles, CA 90024-1567		
8. AUTHOR(S) M. Ashour-Abdalla P.L. Pritchett D. Schriver		9. SPONSORING/MONITORING AGENCY NAME(S) AND ADDRESS(ES) Phillips Laboratory 29 Randolph Road Hanscom AFB, MA 01731-3010  Contract Manager/Gregory Ginet/GPSG		
10. SPONSORING/MONITORING AGENCY REPORT NUMBER  PL-TR-93-2112		11. SUPPLEMENTARY NOTES		
12a. DISTRIBUTION/AVAILABILITY STATEMENT  Approved for public release; distribution unlimited		12b. DISTRIBUTION CODE		
13. ABSTRACT (Maximum 200 words) The basic physical processes that occur during the active electron beam experiments in the ionosphere are examined using multi-dimensional particle simulations. A three-dimensional isolated-system, electrostatic model is used to establish the characteristic time scales associated with injection and to investigate the processes of spacecraft charging and the loss of coherence during beam propagation. Two-dimensional electromagnetic simulations indicate that the beam-plasma interaction leads to the formation of a current structure which acts like an antenna and emits whistler waves in a coherent manner. An ion emitter instrument which injects indium ions will be used during the Geotail and Cluster satellite missions to control the spacecraft potential to be near that of the ambient plasma. To understand the beam-plasma interaction that can occur due to the ejection of the ion beam into various regions of the Earth's magnetosphere, a linear theory study is presented to see whether particular combinations of ambient plasma parameters and ion beam emission modes exist, such that plasma instabilities may be excited.				
14. SUBJECT TERMS Beam injection, Spacecraft charging, Plasma interactions, Computer simulations.		15. NUMBER OF PAGES 50		16. PRICE CODE
17. SECURITY CLASSIFICATION OF REPORT Unclassified	18. SECURITY CLASSIFICATION OF THIS PAGE Unclassified	19. SECURITY CLASSIFICATION OF ABSTRACT Unclassified	20. LIMITATION OF ABSTRACT SAR	



## TABLE OF CONTENTS

LIST OF FIGURES.....	v
LIST OF TABLES.....	vii
1. ELECTRON BEAM EXPERIMENTS.....	1
2. ISOLATED- SYSTEM SIMULATION MODEL IN 2D AND 3D.....	2
3. CHARACTERISTIC INJECTION TIME SCALES.....	5
4. SPACECRAFT CHARGING.....	7
5. BEAM PROPAGATION.....	10
6. WHISTLER MODE RADIATION FROM DC ELECTRON BEAMS.....	17
6.1. Initial-Value Model.....	17
6.2 Radiation from an Injected Beam.....	24
7. SPACECRAFT POTENTIAL CONTROL VIA INDIUM ION BEAM INJECTION.....	27
8. OPERATING PRINCIPLES OF THE LIQUID METAL ION SOURCE (LMIS).....	29
9. LINEAR THEORY.....	30
10. SUMMARY.....	38
REFERENCES.....	39

For
<input checked="" type="checkbox"/>
<input type="checkbox"/>
<input type="checkbox"/>

DTIC QUALITY INSPECTED 6

By.....	
Distribution.....	
Availability Codes	
Dist	Avail and/or Special
A-1	



## LIST OF FIGURES

1. Configuration used in the isolated-system simulation model in two and three dimensions. The rectangular-shaped spacecraft is immersed in a uniform ambient plasma, and the uniform magnetic field points in the  $x$  direction. The beam electrons are emitted from one side of the spacecraft. For a typical rocket experiment the grid spacing  $D$  corresponds to about 20 cm ..... 3
2. Time history of the spacecraft potential  $\Phi_c$  (normalized to the beam energy  $m_e v_b^2/2$ ) for injection into vacuum for two different size craft ..... 8
3. Time histories of (a) the spacecraft potential  $\Phi_c$  (normalized to the beam energy  $m_e v_b^2/2$ ) and (b) the return current to the spacecraft  $I_r$  (normalized to the injection current  $I_0$ ) for different values of the ambient to beam density ratio  $n_{e0}/n_{b0}$ . ..... 9
4. The  $v_x - x$  phase space for the beam electrons for injection into an ambient plasma with density given by  $n_{e0}/n_{b0} =$  (a) 0.25, (b), 0.10, (c) 0.025. In Figure 4a the time  $\omega_{pb}t = 130$ , while in Figures 4b and 4c,  $\omega_{pb}t = 140$  ..... 11
5. (a) The electrostatic potential  $\Phi(x)$  (normalized to the beam energy  $m_e v_b^2/2$ ) at  $y = L_y/2$ ,  $z = L_z/2$  at time  $\omega_{pb}t = 130$  for injection into an ambient plasma with density given by  $n_{e0}/n_{b0} = 0.25$ . (b) The corresponding power spectrum of the potential computed at  $x/\Delta = 406$ ,  $y = L_y/2$ ,  $z = L_z/2$ . ..... 13
6. Scatter plots of the location of the beam electrons at time  $\omega_{pb}t = 100$  for injection at  $45^\circ$  to the magnetic field. (a)  $x$ - $y$  scatter plot for all electrons; (b)  $y$ - $z$  scatter plot for electrons in the range  $128 < x/\Delta < 188$ ; (c)  $y$ - $z$  scatter plot for electrons in the range  $248 < x/\Delta < 308$  ..... 14
7. Time histories of the perpendicular electric field  $E_y$  (left-hand side) and the corresponding power spectra (right hand side) for the same conditions as in Figure 6. The fields are measured at  $x/\Delta = 218$ ,  $z = L_z/2$  and (a,b)  $y/\Delta = 33$  (inside the beam cylinder), (c,d)  $y/\Delta = 45$  (outside the beam cylinder) ..... 15
8. A schematic of the initial-value simulation model. The initial beam and return currents are field aligned and confined to the central portion (in  $x$ ) of the simulation box ..... 18

9. Time histories of (a) the y component of the electrostatic field energy for mode 7 and (b,c) the z component of the magnetic field energy for modes 1 and 2. . . . . 20
10. Power spectra computed in the ambient plasma region at  $x/\Delta = 80$  and 176 averaged over all values of y for (a)  $B_y$ , (b)  $B_z$ , and (c)  $E_z$ . . . . . 21
11. Time histories of  $|J_y(k_y)|^2$  and  $|J_z(k_y)|^2$  in the beam region for (a) mode 1 and (b) mode 2. . . . . 23
12. Contours of the  $B_z$  magnetic field resulting from the injection of an electron beam located at  $x/\Delta = 245$  and  $y/\Delta = 64$  into an ambient plasma with  $\Omega_e/\omega_{pe} = 0.5$ . Solid contours indicate positive values of  $B_z$ , while dotted contours indicate negative values . . . . . 25
13. Power spectra for the  $B_y$ ,  $B_z$ , and  $E_{Ty}$  fields averaged over the interval  $0 < \omega_{pbt} < 200$  at a point  $\delta x/\Delta = 90$ ,  $\delta y/\Delta = 40$  away from the source of the electron beam. The ambient density is given by  $\Omega_e/\omega_{pe} = 0.5$ . . . . . 26
14. This figure shows the dispersion of low frequency waves found from numerical solutions of the general warm plasma dispersion relation for an indium ion beam emitted while the satellite is in the plasma sheet boundary layer. Plotted is frequency (normalized to the background ion gyrofrequency) versus wavenumber (times the electron Debye length). The solid line corresponds to the real frequency and the growth rates are shown by the dashed line for three different wave propagation angles. Note the growth rate maximizes for transverse wave propagation. . . . . 33
15. The wave dispersion relation when the indium beam is emitted in the central plasma sheet. The format is the same as Figure 14, but here the ratio  $U/v_{tb}$  is varied and the lowest value where there is still an appreciable instability is shown. The background plasma parameters are found in Table 2. In this case, if  $U/v_{tb}$  falls below 6, no instability is possible . . . . . 34
16. Dispersion relation for beam emission in the plasma sheet boundary layer. The format is the same as in Figure 15, with the background parameters found from Table 2. . . . . 35
17. Dispersion relation for beam emission in the solar wind. The format is the same as in Figure 15, with the background parameters found from Table 2 . . . . . 36

18. Dispersion relation for beam emission in the lobe. The format is the same as in Figure 15, with the background parameters found from Table 2. Note that this region has the highest threshold for instability compared to the others ..... 37

### TABLES

1. Stagnation time  $t_s$  as a function of the dimensionless beam velocity  $v_b$  ..... 6
2. Typical observed parameters for each of the four regions under consideration ..... 30



## 1. ELECTRON BEAM EXPERIMENTS

The procedure of injecting artificial electron beams in space in order to probe the ionosphere and magnetosphere and to conduct studies in basic plasma physics was initiated more than two decades ago. In January 1969 *Hess et al.* [1971] launched a rocket-borne electron accelerator from Wallops Island. At an altitude of a few hundred kilometers the accelerator ejected a series of electron-beam pulses up to 1 s in duration downward along the magnetic field line. The electron energy ranged up to 9.5 keV, and the current was varied up to a maximum of 490 mA. The highest power pulses produced auroral rays in the upper atmosphere which were detected on the ground by sensitive optical systems. This experiment demonstrated the feasibility of propagating electron beams long distances in space with apparently relatively small alterations resulting from plasma instabilities or beam propagation problems. In the intervening years this technique of "active" experiments has been developed considerably and has come to play an increasingly important role in space physics research. For a comprehensive review of this progress see the recent article by *Neubert and Banks* [1992].

There have been two main themes to the active beam experiments. The first is to serve as a probe of naturally occurring fields on either a local (*e.g.*, the GEOS 1 and 2 experiments [*Melzner et al.*, 1978; *Junginger et al.*, 1984]) or global (*e.g.*, the ECHO series of experiments [*Winckler*, 1980, 1990]) scale. In recent years, however, a second theme has become increasingly dominant: determining the detailed physics of beam-plasma interactions. This involves a number of fundamental plasma processes, many of them of a highly nonlinear nature: spacecraft charging, beam dynamics, beam interactions with neutral gas and ambient plasma, and the generation of electromagnetic waves from continuous and pulsed beams.

Active experiments in space offer both advantages and disadvantages compared to laboratory experiments. Among the advantages are that the spatial scales are much larger and that one can conduct studies free from the contaminating effects of nearby chamber walls. The major disadvantage is that diagnostic capabilities are much more limited. This latter drawback has been partially overcome in recent years by the development of increasingly realistic simulation models which can provide

a global perspective on the various processes involved in the beam-injection experiments. These models can thus serve as an important complement to the actual observations, which are obtained on one, or at most a few, spacecraft.

In this report we review our progress in employing three-dimensional electrostatic and two-dimensional electromagnetic particle simulations to investigate the basic physical processes that occur during active electron beam experiments in the ionosphere.

## 2. ISOLATED-SYSTEM SIMULATION MODEL IN 2D AND 3D

In early simulation models of beam-plasma interactions [see, *e.g.*, Dawson and Shanny, 1968] it was customary to assume periodic boundary conditions along the direction of beam propagation. This meant that one was considering only a small portion of a much longer (strictly, infinite length) beam. Such a model is clearly inappropriate for space experiments where a paramount question concerns the ability of the beam to propagate away from the near environment of the electron gun source. In simulations with one spatial dimension, it is straightforward to implement a nonperiodic geometry [see, *e.g.*, Katz *et al.*, 1986; Okuda *et al.*, 1987; Winglee and Pritchett, 1987]. Such models, however, are restricted to studies of field-aligned injection. In this section we describe the development of an isolated-system electrostatic simulation model in two (BIG) and three (BIG3D) spatial dimensions [Pritchett and Winglee, 1987; Winglee and Pritchett, 1988; Pritchett, 1991].

The basic configuration of the model is illustrated in Figure 1 for the 2D case. The spacecraft, beam, and ambient plasma are treated as an isolated system. The ambient magnetic field is assumed to be uniform and points in the  $x$  direction. The spacecraft has an idealized rectangular shape and is immersed in a uniform ambient plasma. It is located well away from any boundaries, so that it can draw return currents from all sides. The solution of Poisson's equation for the electrostatic potential is obtained by convolving the Fourier transform of the charge density on the 2D or 3D grid with that of the Green's function for a single particle. The surface of the spacecraft is treated as an equipotential, which is accomplished through the use of the capacitance matrix [Hockney, 1968]. The beam

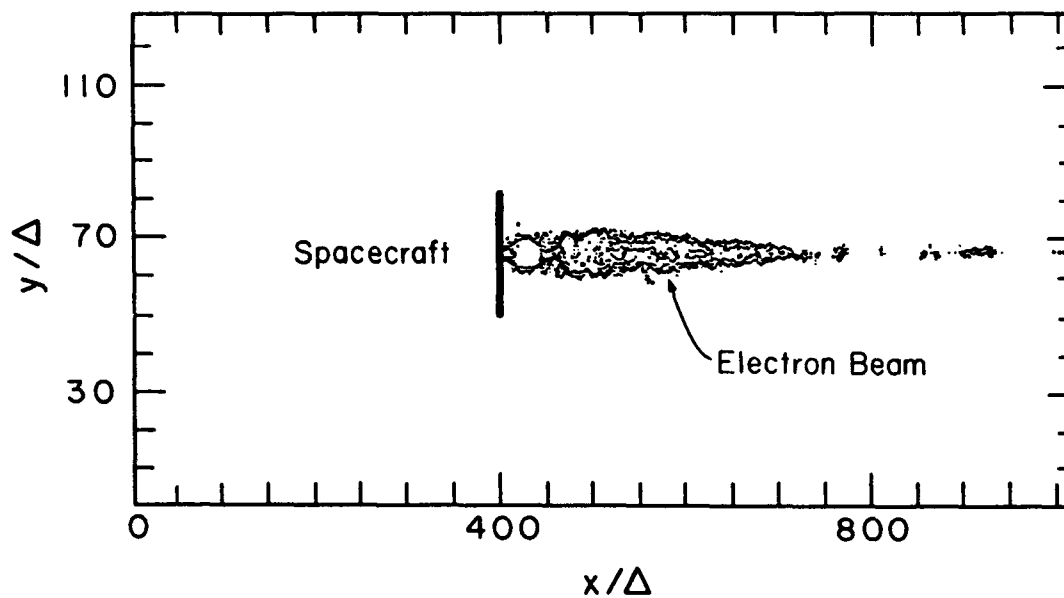


Figure 1. Configuration used in the isolated-system simulation model in two and three dimensions. The rectangular-shaped spacecraft is immersed in a uniform ambient plasma, and the uniform magnetic field points in the  $x$  direction. The beam electrons are emitted from one side of the spacecraft. For a typical rocket experiment the grid spacing  $\Delta$  corresponds to about 20 cm.

electrons are injected from one side of the spacecraft with a monoenergetic velocity distribution at any angle relative to the magnetic field. For each electron injected into the plasma, the spacecraft is given an opposite charge. If a plasma particle or a returning beam electron strikes the spacecraft, it is removed from the system and its charge is added to that on the spacecraft.

It is not possible to model precisely the various length scales and density ratios present in the injection experiments. Thus, the beam typically has an initial width of a few centimeters, while the rocket has a length of several meters. The beam density at injection is of the order of  $10^7 \text{ cm}^{-3}$ , while the ambient plasma density is only of the order of  $10^5 \text{ cm}^{-3}$ . In the 3D model the rocket length is usually  $16\Delta$ , so that the grid spacing  $\Delta \sim 20 \text{ cm}$ . The minimum beam area that can be resolved is  $2\Delta \times 2\Delta = 4\Delta^2$ . This is considerably larger than the actual area. We shall thus require only that the total injected current in the simulation be the same as the experimental value  $I_0$ . As a consequence, the injection density in the simulation will be smaller than the actual value. By matching to the beam energy  $E_b$  and  $I_0$ , we find that the dimensionless beam velocity  $\tilde{v}_b \equiv v_b/\Delta\omega_{pb}$  in the simulations is given by

$$\begin{aligned}\tilde{v}_b &= (4 m_e \epsilon_0 v_b^3 / e I_0)^{1/2} \\ &= 1.15 (E_b / \text{keV})^{3/4} / (I_0 / \text{Amp})^{1/2}.\end{aligned}\quad (1)$$

Thus, for a 1-keV, 50-mA beam, which was typical for the CHARGE 2 [Myers *et al.*, 1989] and Spacelab 2 [Gurnett *et al.*, 1986] experiments,  $\tilde{v}_b = 5.15$ . In contrast, for the ECHO 7 experiments [Winckler *et al.*, 1989], where a much higher beam energy was employed (40 keV, 250 mA),  $\tilde{v}_b = 36.7$ . For the CHARGE 2B mission involving a 3-keV, 2-A beam [J. Ernstmeier, private communication, 1990],  $\tilde{v}_b = 1.86$ .

The typical simulation grid dimensions in the 3D model are  $N_x \times N_y \times N_z = 512 \times 32 \times 32$ . The grid spacing in the x direction can be stretched to  $\Delta x = 2\Delta$  so that the simulation can be run for longer times before the beam reaches the boundary. This feature is employed only when it is not necessary to resolve spatial dimensions on the order of the beam Debye length  $\lambda_{Db} = \tilde{v}_b \Delta$  near the spacecraft.

The electrons and ions comprising the ambient plasma are represented by superparticles. For the plasma electrons, the charge-to-mass ratio is the same as for the beam electrons, and the charge is adjusted so that the initial density of the plasma relative to the injected beam density has the desired value  $n_{e0}/n_{b0}$ . The mass of the plasma ions is taken to be 100 times the mass of the plasma electrons. The initial velocity distributions of the plasma electrons and ions are Maxwellians with  $T_e = T_i$  and a typical thermal velocity  $v_{Te} = 0.1 v_b$ . With a superparticle density of one per  $\Delta^3$  cell, the ambient plasma is represented by just over 1 million electrons and ions each.

### 3. CHARACTERISTIC INJECTION TIME SCALES

There are two characteristic time scales which determine the ability of the beam to escape from the near environment of its source [Winglee and Pritchett, 1987; Pritchett and Winglee, 1987]. The first is the beam stagnation time  $t_s$ . This is defined to be the time required for the first beam electron to be brought to rest under the influence of the positively-charged spacecraft for injection into vacuum. The corresponding distance away from the injection point where the first electron comes to rest is called the stagnation distance  $x_s$ . In one dimension (the case of an infinitely wide beam),  $t_s = 2 \omega_{pb}^{-1}$  independent of the beam velocity, and  $x_s = 0.5 \lambda_{Db}$ . In two dimensions, the stagnation time depends on  $\tilde{v}_b$  approximately as  $\tilde{v}_b^{1/2}$  and also varies somewhat with beam width and spacecraft size [Winglee and Pritchett, 1988]. A typical value was  $t_s = 9 \omega_{pb}^{-1}$ , with  $x_s = 1.3 \lambda_{Db}$ .

The variation of  $t_s$  as a function of the dimensionless velocity  $\tilde{v}_b$  in three dimensions is shown in Table 1. In these simulations the spacecraft dimensions are  $L_x \times L_y \times L_z = 4\Delta \times 16\Delta \times 8\Delta$ , and the ambient magnetic field strength is assumed to be such that  $\Omega_e/\omega_{pb} = 1$ . The most dramatic feature of the results in Table 1 is that the values for  $t_s$  are much larger than the corresponding results in two dimensions. Thus, for  $\tilde{v}_b = 5$ ,  $\omega_{pb} t_s = 64$ , compared to 8.3 for a  $4\Delta \times 16\Delta$  spacecraft in two dimensions. The reason for this substantial change is that in three dimensions the electric field for a point charge falls off as  $1/r^2$ , whereas in two dimensions the decrease is only as  $1/r$ . It is apparent that the stagnation time increases linearly with  $\tilde{v}_b$ . If we extrapolate to the value  $\tilde{v}_b = 36.7$  corresponding to the peak ECHO

7 beam energy, we find  $\omega_{pb}t_s \approx 460$ . The stagnation distance  $x_s$  relative to the beam Debye length increases only slightly for the range of  $\tilde{v}_b$  values shown in Table 1, from  $x_s/\lambda_{Db} = 3.0$  for  $\tilde{v}_b = 2$  to 3.9 for  $\tilde{v}_b = 8$ .

TABLE 1. Stagnation Time  $t_s$  as a Function of the Dimensionless Beam Velocity  $\tilde{v}_b$

$\tilde{v}_b$	$\omega_{pb}t_s$
2	22
3	37
4	51
5	64
8	100

The values of the stagnation time depend sensitively on the true three-dimensional variation of the electrostatic field. In a pseudo-three-dimensional model in which periodic boundary conditions are assumed in the  $y$  and  $z$  directions, there will be repeated images of the positively charged spacecraft. These image charge distributions will modify the spatial dependence of the electric field. Thus, with a spacecraft length  $L_y = 16\Delta$  and a periodicity length of  $32\Delta$  in  $y$ , the value of  $\omega_{pb}t_s$  for  $\tilde{v}_b = 4$  is reduced from 51 to 25.

The second characteristic time scale associated with the beam injection is the plasma response time  $t_{rp}$ . This is the time required for the ambient plasma to respond to the fields produced by the injection of the electron beam.  $t_{rp}$  is determined by the ambient density,  $t_{rp} \approx \sqrt{3}/\omega_{pe}$ , where  $\omega_{pe}$  is the ambient plasma frequency. The relative value of  $t_s$  and  $t_{rp}$  determines two characteristic injection regimes. When  $t_s$  is the shorter time, there is not sufficient time for return currents to flow and neutralize the spacecraft before the stagnation region forms. In this case there will be strong vehicle charging and low injection efficiency. If, on the other hand,  $t_{rp}$  is the shorter time, then the spacecraft will be neutralized before the stagnation region has a chance to form. In this case the injection efficiency will be high.

#### 4. SPACECRAFT CHARGING

Figure 2 shows the spacecraft potential  $\Phi_c$  as a function of time for the case of  $\bar{v}_b = 4$ ,  $\Omega_e/\omega_{pb} = 0.5$ , and for  $4\Delta \times 16\Delta \times 4\Delta$  and  $2\Delta \times 8\Delta \times 2\Delta$  spacecraft situated in vacuum. With no ambient return current,  $e\Phi_c$  increases basically linearly in time up past the beam energy. For the smaller craft the stagnation time is shorter ( $27 \omega_{pb}^{-1}$  as opposed to  $50 \omega_{pb}^{-1}$ ), and so the potential rises more rapidly. The charging above the beam voltage after stagnation is greater for the smaller spacecraft, where the final spacecraft potential is some 50% above the beam value. This occurs because beam electrons are scattered in the stagnation region onto adjacent field lines. With a small craft, a larger fraction of these field lines do not intersect the craft, and so these electrons will not be returned to neutralize the source. This results in a higher potential. Such charging up to and above the beam voltage has been observed during the SEPAC experiments [Obayashi *et al.*, 1985; Sasaki *et al.*, 1986] when the conductive surfaces of the orbiter were out of contact with the ambient plasma and during rocket experiments at times of extremely low ambient plasma density. In the MAIMIK experiment [Maehlum *et al.*, 1988], the electron gun was located on the daughter which had a surface area of only  $1.1 \text{ m}^2$ . This small area, together with the reduced plasma density of  $10^4 \text{ cm}^{-3}$ , is evidently responsible for the observed charging of up to 1.6 times the beam voltage.

Figure 3a shows the time history of the spacecraft potential for injection into an ambient plasma for three different values of the ratio  $n_{e0}/n_{b0}$  of ambient to beam density. For  $n_{e0}/n_{b0} = 0.25$ ,  $e\Phi_c$  never exceeds 5% of the beam energy; for  $n_{e0}/n_{b0} = 0.10$ ,  $e\Phi_c$  initially grows rapidly to 10% of the beam energy but then increases more slowly with time as the return current flows partially neutralize the charge accumulation on the spacecraft. For the low density case of  $n_{e0}/n_{b0} = 0.025$ ,  $e\Phi_c$  maintains a rapid increase throughout the run and exceeds the beam energy for  $\omega_{pb}t > 115$ .

Figure 3b shows the time history of the return current to the spacecraft for the highest- and lowest-density cases. Since no beam electrons return to the spacecraft, the return current is provided entirely by the ambient plasma. The total thermal current to the spacecraft  $I_T$ , divided by the injection current  $I_0$  is found to be  $I_T/I_0 = 2.9 n_e/n_{b0}$ . Thus for all three

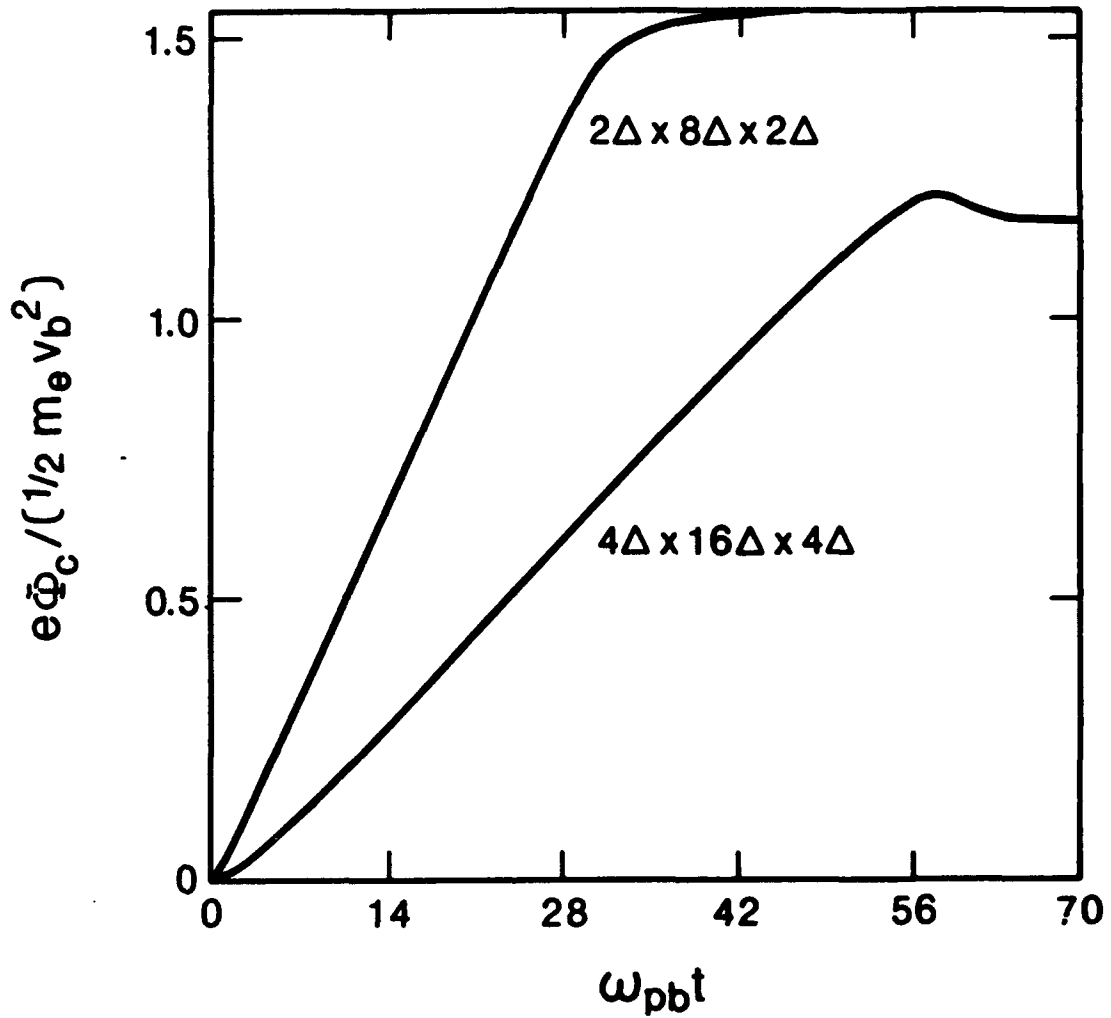


Figure 2. Time history of the spacecraft potential  $\Phi_c$  (normalized to the beam energy  $m_e v_b^2/2$ ) for injection into vacuum for two different size craft.

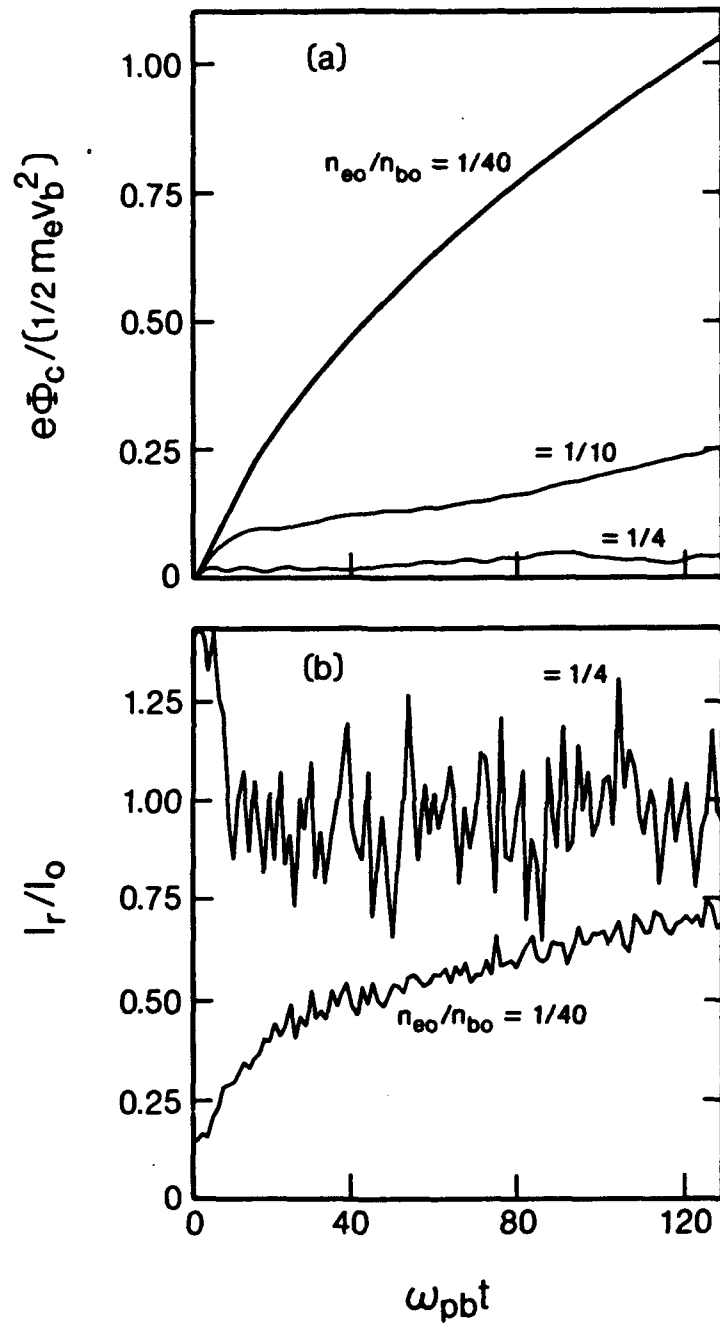


Figure 3. Time histories of (a) the spacecraft potential  $\Phi_c$  (normalized to the beam energy  $m_e v_b^2/2$ ) and (b) the return current to the spacecraft  $I_r$  (normalized to the injection current  $I_0$ ) for different values of the ambient to beam density ratio  $n_{e0}/n_{b0}$ .

density ratios considered here,  $I_T/I_0 < 1$ . For  $n_{e0}/n_{b0} = 0.25$ ,  $I_0$  is some 40% larger than  $I_T$ , and this small excess of injection current can be balanced by a very low-level charging of the spacecraft, as can be seen from Figure 3. For  $n_{e0}/n_{b0} = 0.10$ , the observed return current is about  $3I_T$ , and this current can be collected as a result of a moderate charging of the spacecraft. For  $n_{e0}/n_{b0} = 0.025$ , the actual return current can only approach  $I_0$  by charging the spacecraft up to the beam potential. It is thus clear that the thermal current  $I_T$  should not provide the limit to the injection current that can propagate away from the vicinity of the source. The degree of charging of the spacecraft will be determined by the need to balance  $I_0$ . Clearly, the larger the conducting area of the spacecraft, the smaller will be the potential.

There is, however, a limit on the amount of current that can be injected. As  $I_0$  is increased, the parameter  $\tilde{v}_b$  decreases, and hence the stagnation time decreases. If  $t_s$  becomes comparable to the plasma response time, then the beam will be brought to rest before the return current flows can control the spacecraft charging. The precise condition is  $t_s = 2 t_{rp}$  [Pritchett, 1991], which occurs in the present simulations for  $\tilde{v}_b = 2$ .

## 5. BEAM PROPAGATION

We now consider the propagation of the beam away from the spacecraft. Figure 4 shows  $v_x$ - $x$  phase spaces at late times for the case of parallel injection for  $\tilde{v}_b = 4$ ,  $\Omega_e/\omega_{pb} = 0.5$ , and a  $4\Delta \times 16\Delta \times 4\Delta$  spacecraft for density ratios  $n_{e0}/n_{b0} = (a) 0.25$ ,  $(b) 0.10$ , and  $(c) 0.025$ . The ratio  $n_{e0}/n_{b0} = 0.25$  corresponds to an ambient density of  $1.3 \times 10^5 \text{ cm}^{-3}$ , which is a typical ionospheric value. For the two higher ambient densities (Figures 4a and 4b), the beam initially propagates away at the injection velocity. After a distance of  $\sim 80\Delta$ , a coherent wave structure begins to appear which is then further amplified. This leads to the formation of large trapping vortices in which some of the beam electrons have their parallel velocity reduced to zero. In the region of the first complete vortex the beam suffers an abrupt transverse disruption.

Figure 5a shows the potential  $F$  as a function of  $x$  for  $y = L_y/2$ ,  $z = L_z/2$  for the  $n_{e0}/n_{b0} = 0.25$  case. For a distance of  $\sim 60\Delta$  in front of the spacecraft (the injection point of the beam is  $x = 256$ ) the potential is very small and

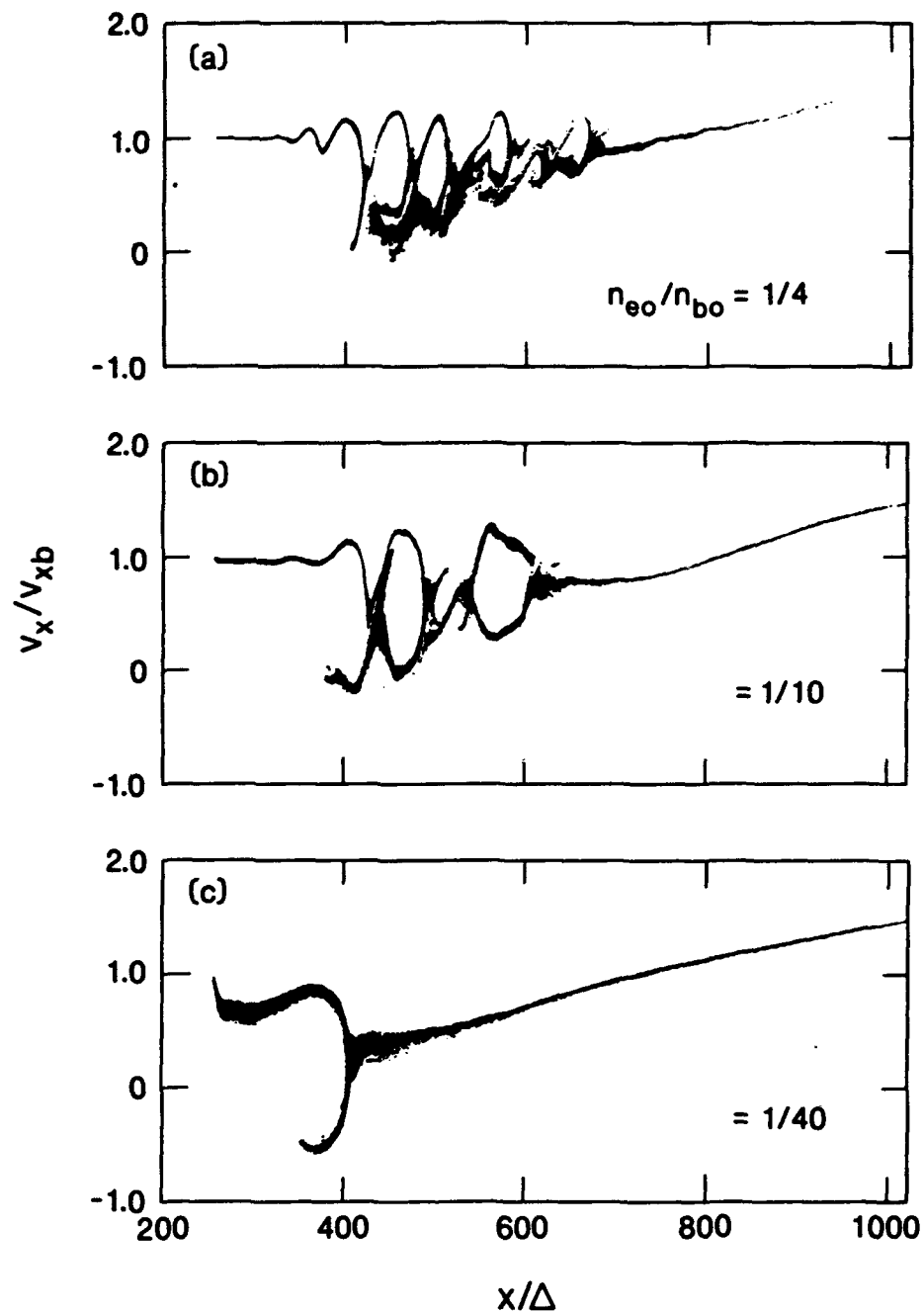


Figure 4. The  $v_x - x$  phase space for the beam electrons for injection into an ambient plasma with density given by  $n_{e0}/n_{b0} =$  (a) 0.25, (b), 0.10, (c) 0.025. In Figure 4a the time  $\omega_{pb}t = 130$ , while in Figures 4b and 4c,  $\omega_{pb}t = 140$ .

nearly constant. This indicates that initially the beam is well neutralized. A rapid modulation of  $\Phi(x)$  then grows up and decays away over the range  $350 \leq \Delta \leq 650$ . This is the region of the strong trapping vortices (cf. Figure 4a). The peak potentials reach 10–15% of the beam voltage, which is much higher than the spacecraft potential of 3–4%. Figure 5b shows the corresponding power spectrum of the potential computed at the point  $x/\Delta = 406$ ,  $y = L_y/2$ ,  $z = L_z/2$ . The high-frequency oscillations associated with the coherent structures peak at a frequency  $\omega = 0.38 \omega_{pb} = 0.76 \omega_{pe}$ . With a wavelength of  $49\Delta$ , the dispersion relation for the oscillations is found to be  $\omega = 0.74 kv_b$ . The corresponding relation in an infinite plasma with equal beam and plasma densities (which is roughly the situation in the coherent region in the simulations) is  $\omega = kv_b/2$ . The ions are too massive to respond to these high-frequency plasma oscillations. Their gyroradius is large compared to the beam width, and they are able to flow across the magnetic field to neutralize local charge accumulations. This is the origin of the low-frequency peak near the ion plasma frequency in Figure 5b.

We now consider the case where the beam is injected at an angle of  $45^\circ$  to the magnetic field. Figure 6a shows a  $x$ - $y$  scatter plot of the beam electrons at time  $\omega_{pb}t = 100$ . It is apparent that after about 2 or 3 gyroperiods the helical structure of the beam has been destroyed by the space-charge oscillations [Winglee and Pritchett, 1988; Pritchett, 1990]. This loss of parallel coherence is associated with the development of a large spread in the parallel beam velocity caused by the space-charge fields and occurs over a time scale of the order of  $30 \omega_{pb}^{-1}$ . There is also a loss of transverse coherence. Figures 6b and 6c show  $y$ - $z$  scatter plots for the beam electrons in the range  $128 < x/\Delta < 188$  and  $248 < x/\Delta < 308$ , respectively. Near the source the trajectories of the beam electrons form a hollow cylinder. The radius of the cylinder is about equal to the beam gyroradius and has a width of about  $3\Delta$ , which is approximately the beam Debye length. At greater distance from the source (Figure 6c) the cylinder has been filled in, due to the transverse space-charge oscillations excited by the beam. The prediction that the beam electrons should initially lie on a hollow cylinder for the case of low spacecraft charging is consistent with observations during the STS 3 beam experiments [Banks and Raitt, 1988].

Figure 7 shows time histories of the electric field  $E_y$  and the associated power spectra, both inside the beam cylinder (at  $y/\Delta = 33$ , Figures

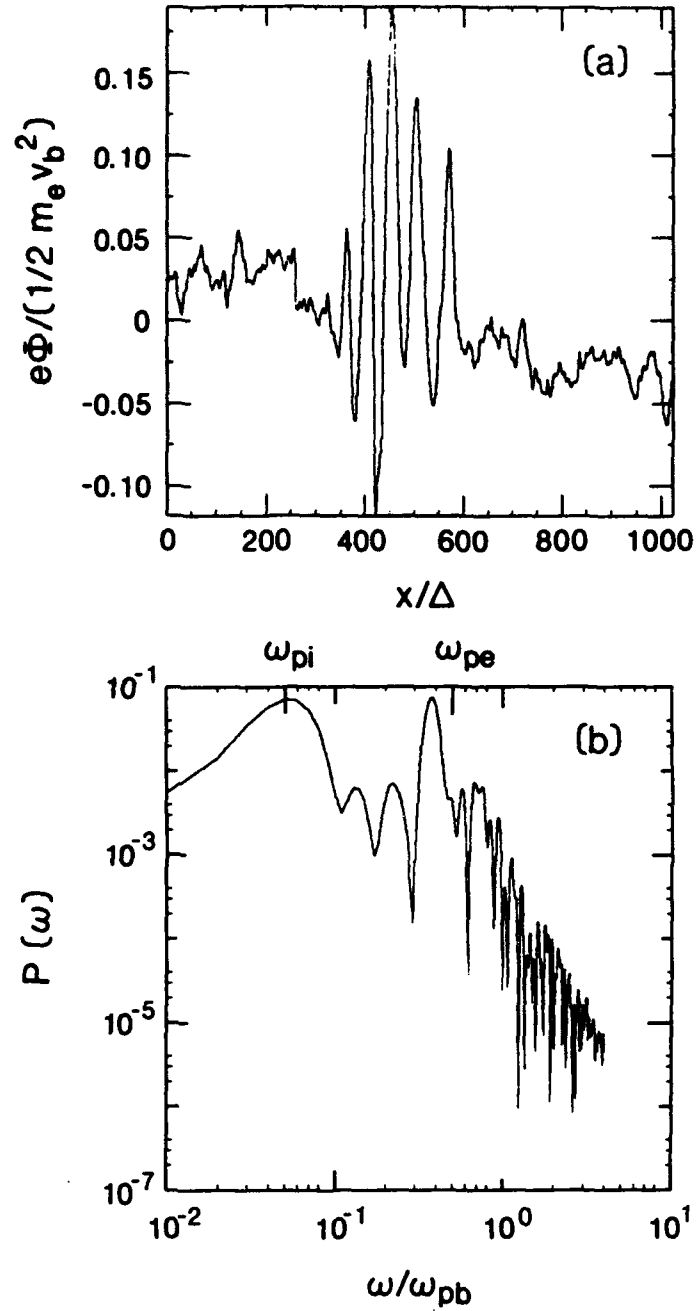


Figure 5. (a) The electrostatic potential  $\Phi(x)$  (normalized to the beam energy  $m_e v_b^2/2$ ) at  $y = L_y/2$ ,  $z = L_z/2$  at time  $\omega_{pb}t = 130$  for injection into an ambient plasma with density given by  $n_{e0}/n_{b0} = 0.25$ . (b) The corresponding power spectrum of the potential computed at  $x/\Delta = 406$ ,  $y = L_y/2$ ,  $z = L_z/2$ .

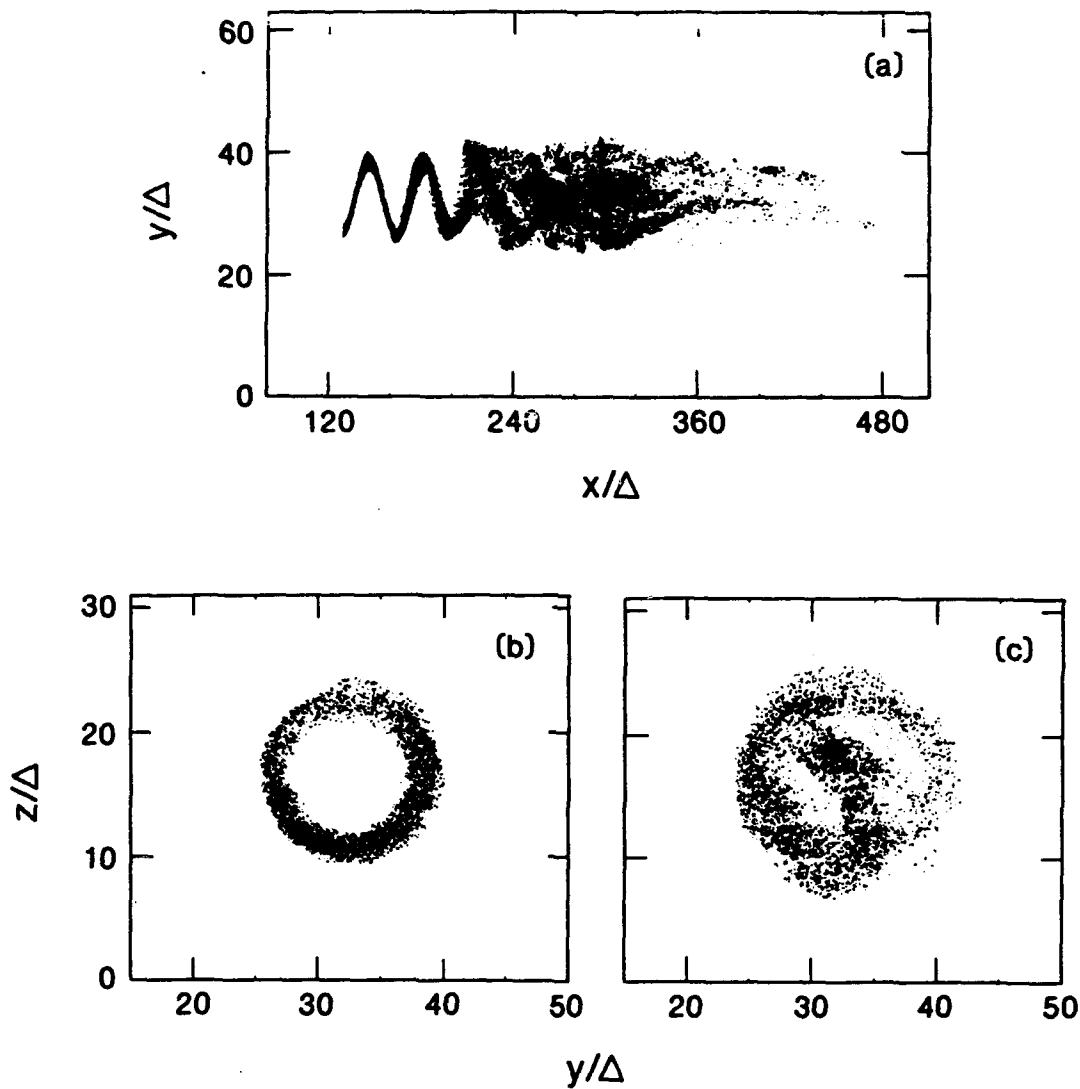


Figure 6. Scatter plots of the location of the beam electrons at time  $\omega_{pb}t = 100$  for injection at  $45^\circ$  to the magnetic field. (a) x-y scatter plot for all electrons; (b) y-z scatter plot for electrons in the range  $128 < x/\Delta < 188$ ; (c) y-z scatter plot for electrons in the range  $248 < x/\Delta < 308$ .

7a, 7b) and outside (at  $y/\Delta = 45$ , Figures 7c, 7d) for  $x/\Delta = 218$  and  $z = L_z/2$ . Inside the beam,  $E_y$  shows an increased oscillation after the beam front has passed at  $\omega_{pbt} \approx 30$ . The spectrum is dominated by a peak slightly below the upper hybrid frequency  $\omega_{UH} = (\omega_{pe}^2 + \Omega_e^2)^{1/2} = 1.4 \omega_{pe}$ . It is presumably these oscillations that produce the transverse spreading of the beam. Outside the beam, the intensity of these high-frequency oscillations is reduced by about a factor of 20. Here the most intense modes are at lower frequencies near the ion plasma frequency.

Thus we conclude that in all the cases considered here the beam is subject to strong distortion or disruption as it propagates away from the spacecraft. These effects are expected to be substantially diminished at low altitudes where the neutral density is high enough so that the effects of ionization need to be included [Winglee, 1990].

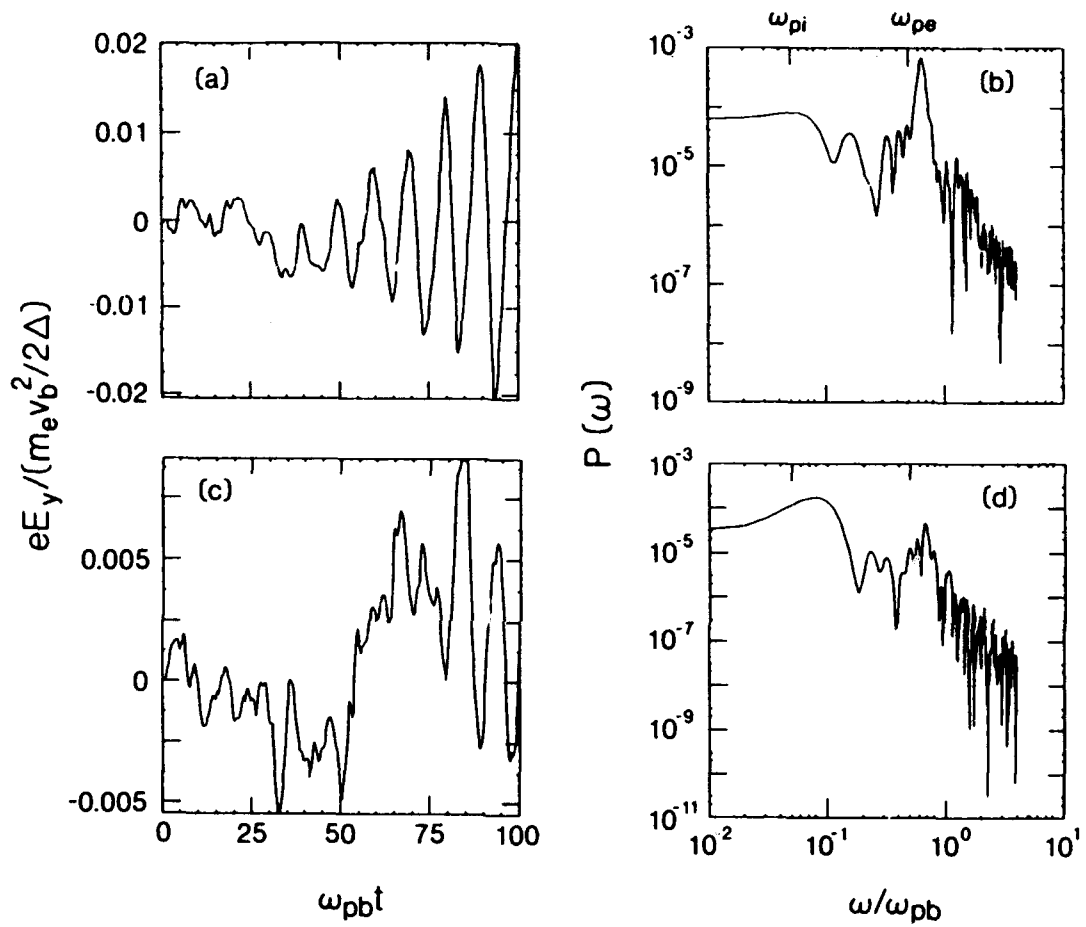


Figure 7. Time histories of the perpendicular electric field  $E_y$  (left-hand side) and the corresponding power spectra (right hand side) for the same conditions as in Figure 6. The fields are measured at  $x/\Delta = 218$ ,  $z = L_z/2$  and (a,b)  $y/\Delta = 33$  (inside the beam cylinder), (c,d)  $y/\Delta = 45$  (outside the beam cylinder).

## 6. WHISTLER MODE RADIATION FROM DC ELECTRON BEAMS

The generation mechanism of the whistler waves observed during the Spacelab 2 mission was not immediately evident. As noted by *Farrell et al.* [1988], the observed wave intensity, which was estimated to be about  $3 \times 10^{-5}$  of the beam power, was of the order of  $10^7$  times greater than expected on the basis of incoherent, single-particle radiation [see, *e.g.*, *Mansfield*, 1967]. Thus some coherent radiation mechanism must have been involved. Since the beam width was less than one whistler wavelength, however, it is difficult to imagine that a conventional whistler instability could produce sufficient amplification within the narrow confines of the beam. *Farrell et al.* [1988] suggested that the mechanism could involve coherent Cerenkov radiation from electron bunching in space at the plasma frequency produced by an electrostatic beam-plasma instability.

In order to simulate the whistler generation process, it is necessary to use an electromagnetic model which includes self-consistent magnetic and inductive electric fields. We describe in this section the results of two-dimensional particle simulations which solve the full set of Maxwell's equations. The initial results, presented in subsection A, use a pure initial-value model for the beam-plasma interaction [*Pritchett et al.*, 1989]. Subsequently, in subsection B, we use the electromagnetic version of the isolated-system model.

### 6.1. Initial-Value Model

Figure 8 gives a schematic diagram of the initial-value simulation model. A dilute beam of field-aligned electrons is assumed to exist initially throughout the central region of the simulation box. In the results presented here, the beam density  $n_{b0}$  is taken to be one quarter of the ambient density  $n_{e0}$ , the beam energy is 5.7 keV, and the width of the beam is 14 m. The current carried by the electron beam must be balanced by a return current in the ambient plasma. To represent this current, we assign an initial drift of  $-v_b/3$  to the ambient electrons located in the beam region (whose density is taken to be  $3n_{e0}/4$ ). Outside the beam region is a stationary ambient plasma of density  $n_{e0}$ . The magnetic field is oriented in the  $y$  direction and has a strength such that  $\Omega_e/\omega_{pe} = 0.3$ . The simulation system

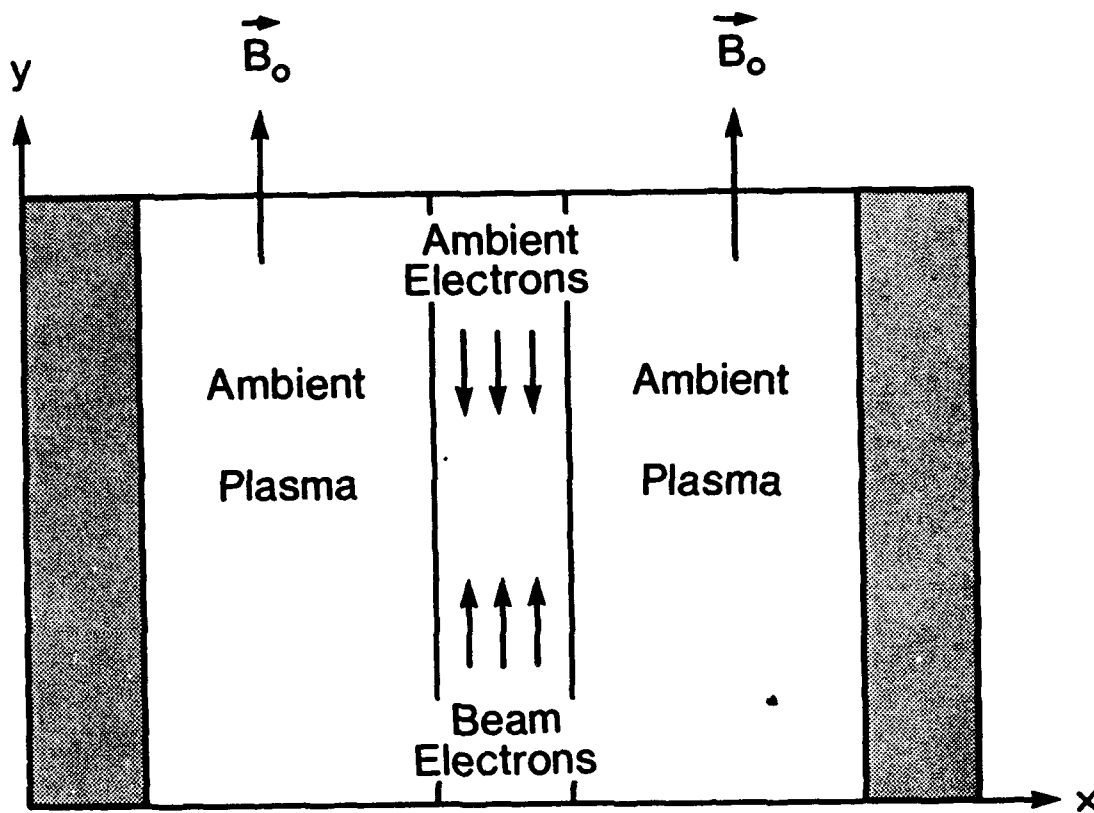


Figure 8. A schematic of the initial-value simulation model. The initial beam and return currents are field aligned and confined to the central portion (in  $x$ ) of the simulation box.

is periodic in  $y$  but bounded in  $x$  and represents a domain of  $220 \text{ m} \times 110 \text{ m}$ . The ions are treated as a fixed neutralizing background.

As is well known, the interaction of a weak beam with an ambient plasma leads to the excitation of electrostatic Langmuir oscillations with wavenumber  $k$  given by  $k \approx \omega_{pe} / v_b$ . In the present simulation this most unstable mode corresponds to mode 7 in the  $y$  direction. Figure 9a shows the time history of the parallel ( $y$ ) component of the electrostatic energy for this mode. The exponential growth is already apparent by  $\omega_{pet} \sim 10$ , and saturation occurs by  $\omega_{pet} \sim 25$ . The linear growth rate is  $0.23 \omega_{pe}^{-1}$ . The growth of the Langmuir oscillations leads to the well-known formation of vortices in the  $v_y$ - $y$  phase space. The Langmuir oscillations are confined to the finite beam region, in agreement with Spacelab 2 observations [Gurnett *et al.*, 1986]. At saturation the total electrostatic field energy amounts to 14% of the initial beam energy. After saturation, the Langmuir waves collapse as the beam-plasma system is thermalized.

Figures 9b and 9c show the time history of the  $z$  component of the magnetic field energy for the two longest wavelength modes in the system (modes 1 and 2 in the  $y$  direction). There is a clear exponential growth phase in both modes that becomes apparent above the background by  $\omega_{pet} \sim 20$ . The rapid growth continues until  $\omega_{pet} \sim 30$ ; subsequently, the field energy remains at an enhanced level. In contrast, the magnetic field energies for modes 3-7 collapse back to the thermal level as the electrostatic waves decay. It is thus clear that persistent long-wavelength electromagnetic modes are being excited on a time scale comparable to that of the beam-plasma interaction.

To identify the nature of these electromagnetic modes, we examine the power spectra curves given in Figure 10. These spectra are measured well outside the beam region. The top two curves are for the  $y$  and  $z$  components of the magnetic field, while the bottom one is for the  $z$  component of the electric field. In all three cases the dashed curve represents the thermal level in the simulation in the absence of an electron beam, while the solid curve is the result with the electron beam. The magnetic plots show enhancements by factors of 80 and 20, respectively, above the thermal level in the frequency range below  $\Omega_e$ . Otherwise, there is no significant wave excitation above the background level. The long-wavelength modes excited by the electron beam are thus clearly whistler waves.

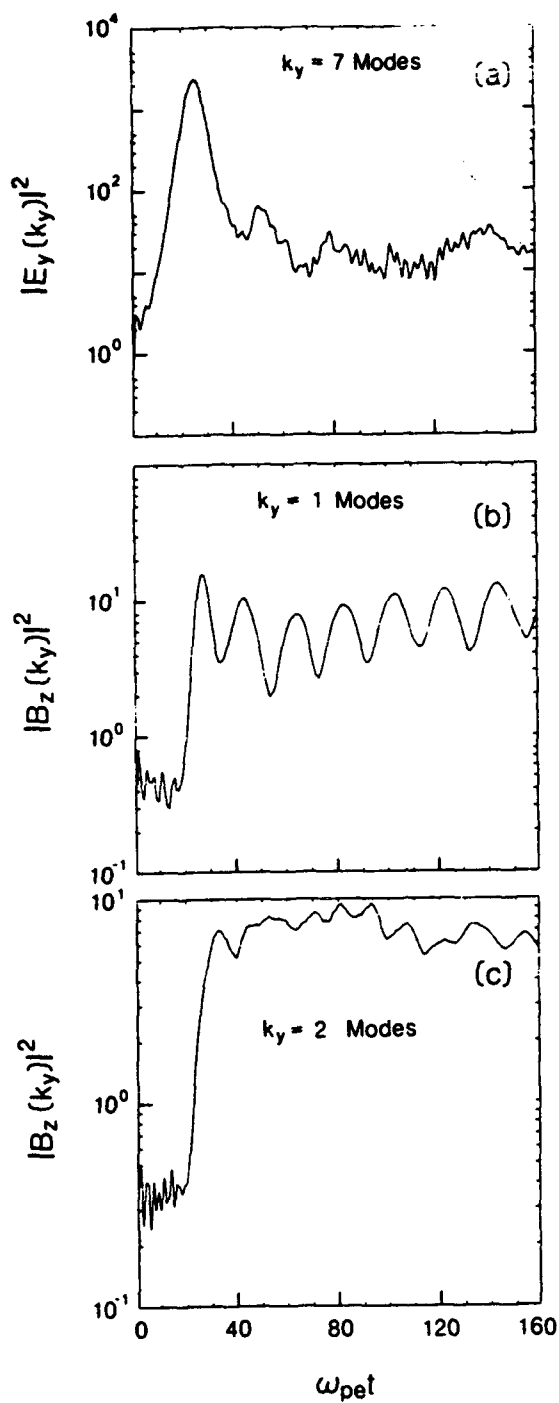


Figure 9. Time histories of (a) the  $y$  component of the electrostatic field energy for mode 7 and (b,c) the  $z$  component of the magnetic field energy for modes 1 and 2.

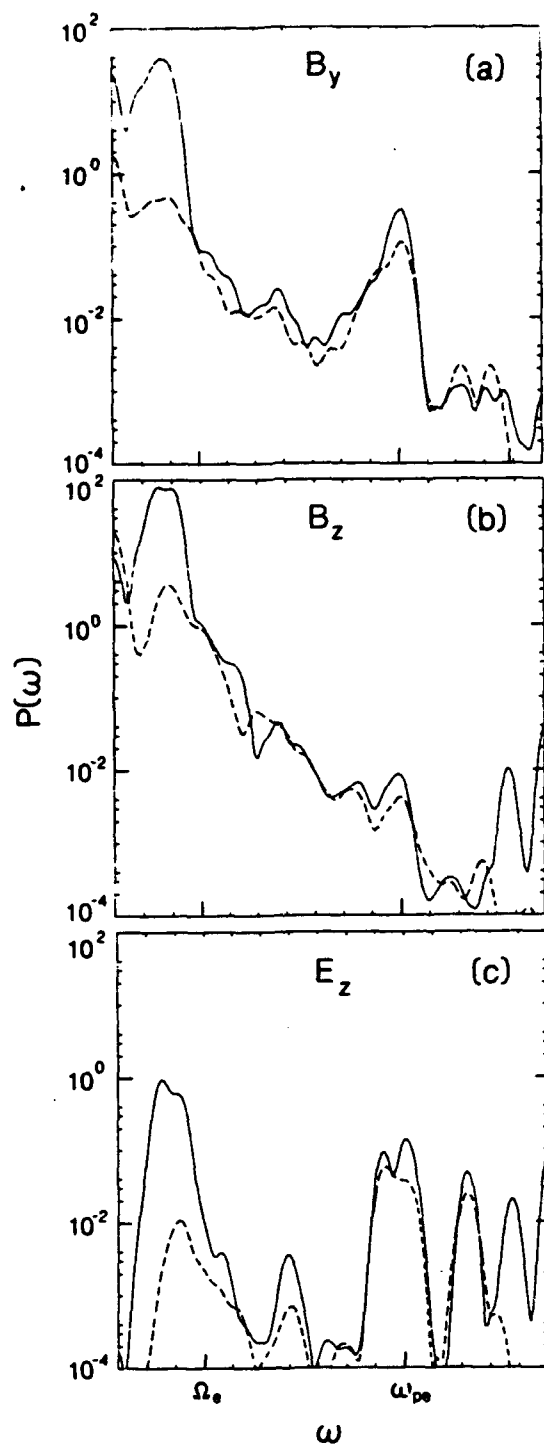


Figure 10. Power spectra computed in the ambient plasma region at  $x/\Delta = 80$  and  $176$  averaged over all values of  $y$  for (a)  $B_y$ , (b)  $B_z$ , and (c)  $E_z$ .

The wave vectors for the four most intense modes excited in the simulation make angles of  $27^\circ$ ,  $45^\circ$ ,  $27^\circ$ , and  $37^\circ$  with respect to the magnetic field and have frequencies  $\omega/\Omega_e = 0.53, 0.50, 0.72$ , and  $0.67$ , respectively. The corresponding resonance cone angles are  $57^\circ$ ,  $59^\circ$ ,  $43^\circ$ , and  $47^\circ$ . Thus the most intense whistler waves are propagating considerably away from the resonance cone. The total energy radiated as whistler waves is estimated to be 0.1% of the initial beam energy.

The present simulations show that the beam-plasma interaction produces a complex current structure with significant  $J_x$ ,  $J_y$ , and  $J_z$  components. While the largest contribution is the mode 7 component associated with the dominant Langmuir wave, there are also substantial contributions in modes 1–6. The transverse components  $J_x$  and  $J_z$  arise from the existence of the electrostatic field in the  $x$  direction which accelerates the electrons perpendicular to the magnetic field and produces  $\mathbf{E} \times \mathbf{B}$  drifts. Figure 11 shows time history plots of  $|J_y(k_y)|^2$  and  $|J_z(k_y)|^2$  for modes 1 (panel *a*) and 2 (panel *b*). The currents are computed from both the beam electrons and the ambient electrons in the original beam region. The dramatic growth in all four cases during the period from  $15\omega_{pe}^{-1}$  to  $30\omega_{pe}^{-1}$  illustrates the common origin of the current structure in the processes associated with the beam-plasma interaction. Although the current structure has significant components in modes 1 through 7, only the first two can satisfy the Cerenkov resonance condition  $k_{\parallel} = \omega/v_{\parallel}$  with  $\omega < \Omega_e$  and  $v_{\parallel} \leq v_b$  and thus produce whistler waves. Since  $|J_{\parallel}|^2 \gg |J_{\perp}|^2$  in the simulations, one surmises that the whistler waves are generated predominantly by the  $J_{\parallel}$  current. This conclusion is further strengthened by the single-particle analysis of *Mansfield* [1967] which shows that  $v_{\perp}$  makes only a small contribution to the Cerenkov radiation level if  $v_{\perp} < v_{\parallel}$ .

The initial-value simulations have thus demonstrated that whistler waves are produced from electron beams on the same time scale as the classical beam-plasma interaction whose dominant feature is the production of intense Langmuir oscillations. The growth of these electrostatic oscillations is accompanied by the formation of a current structure which acts like an antenna and emits whistler waves in a coherent manner. Since the generation efficiency in the simulations is so much higher than that actually observed, however, it is not clear that this

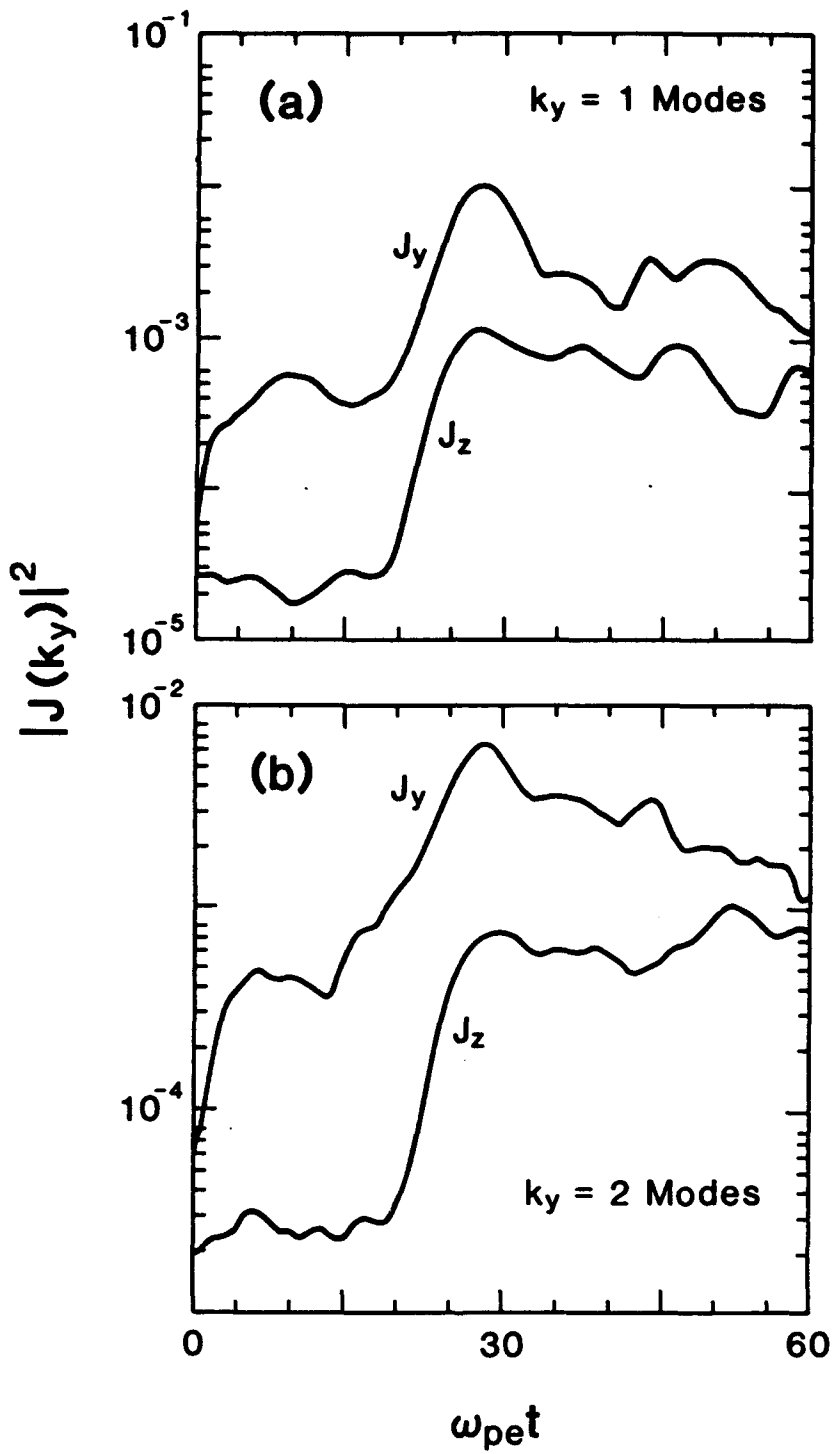


Figure 11. Time histories of  $|J_y(k_y)|^2$  and  $|J_z(k_y)|^2$  in the beam region for (a) mode 1 and (b) mode 2.

mechanism is actually the operative one in the beam experiments in space. We address this point in the next subsection.

## 6.2. Radiation from an Injected Beam

We now use the electromagnetic version of the isolated-system simulation code to reexamine the process of coherent whistler radiation from electron beams. This is a much more realistic model than the initial-value calculation since the beam is now injected at a single point. The configuration is similar to that shown in Figure 1; the beam energy is now higher ( $E_b = 16$  keV), and the grid spacing  $\Delta$  corresponds to about 40 cm. The magnetic field strength will be varied but is always such that the electron cyclotron frequency  $\Omega_e$  is less than the ambient plasma frequency  $\omega_{pe}$ , as was the case during the Spacelab 2 observations.

The most striking difference between the present continuous-injection simulations and the previous initial-value results is the sharply reduced level of electrostatic Langmuir oscillations. Instead of a rapid initial growth followed by collapse of these oscillations, there is now a slower build up of the parallel wave energy toward a quasi-static level on a time scale of 30–40  $\omega_{pb}^{-1}$ . The total electrostatic field energy is now only a few tenths of a percent of the energy of the beam electrons injected during this interval. The initial-value simulations thus appear to have overestimated significantly the strength of the beam-plasma interaction.

Figure 12 shows contours of the perturbed  $B_z$  field at times  $\omega_{pbt} = 40, 80,$  and 120 for the case of  $\Omega_e / \omega_{pe} = 0.5$ . The current sheet formed by the injected electron beam produces an antisymmetric field relative to the beam axis. Superimposed on this dominant field are periodic modulations with a wavelength of  $\sim 90\Delta$ . The direction of propagation relative to the ambient magnetic field appears to decrease as a function of time, from  $\approx 10^\circ$  at the earliest time to  $\approx 4^\circ$  at the latest time. The perturbed  $B_y$  field shows a similar wave pattern. Figure 13 shows power spectra measured at a point  $\Delta x = 90\Delta, \Delta y = 40\Delta$  relative to the beam injection point for the  $y$  and  $z$  components of the magnetic field and the  $y$  component of the transverse (electromagnetic) electric field. The  $B_y$  spectrum shows a clear peak at  $\omega \approx 0.7 \Omega_e$ ; the  $E_y$  spectrum has a similar peak but with an intensity about two orders of magnitude weaker. We thus identify the wave disturbances as

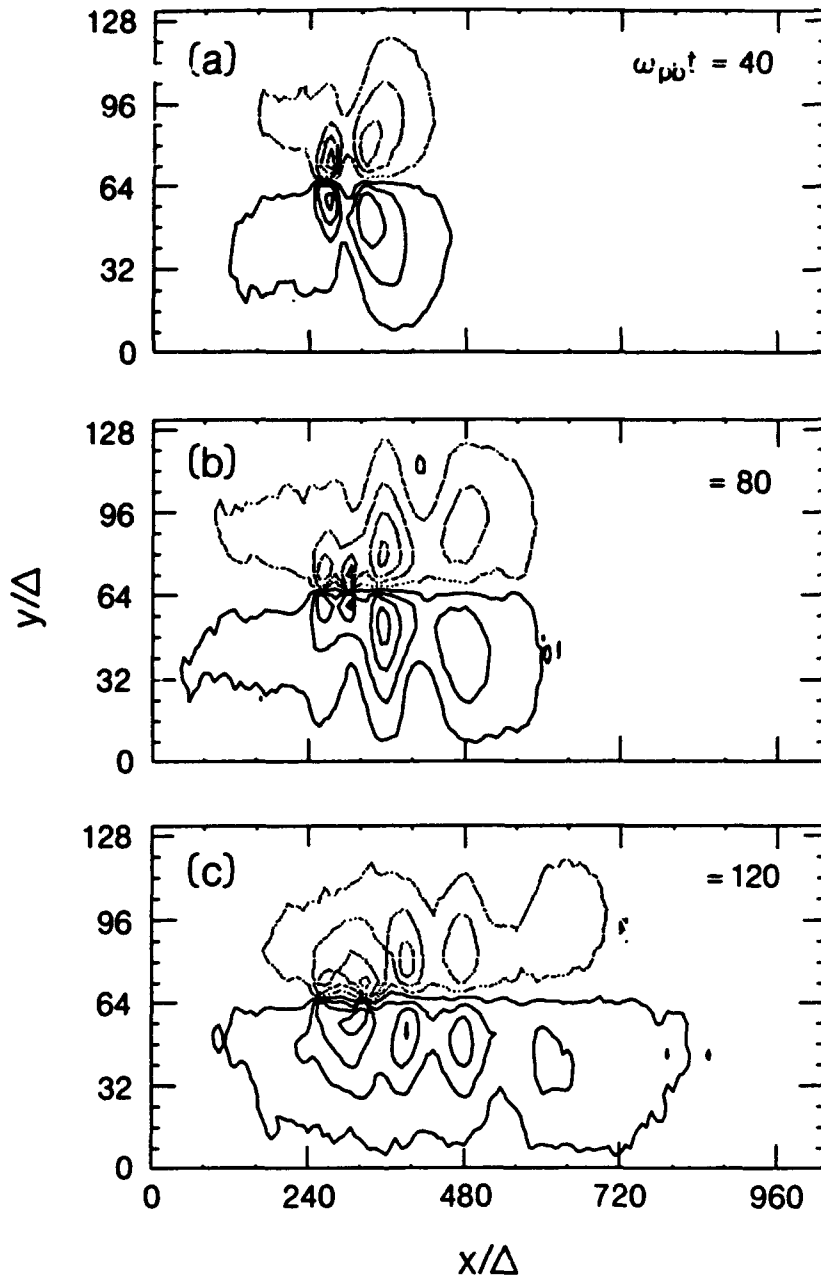


Figure 12. Contours of the  $B_z$  magnetic field resulting from the injection of an electron beam located at  $x/\Delta = 245$  and  $y/\Delta = 64$  into an ambient plasma with  $\Omega_e/\omega_{pe} = 0.5$ . Solid contours indicate positive values of  $B_z$ , while dotted contours indicate negative values.

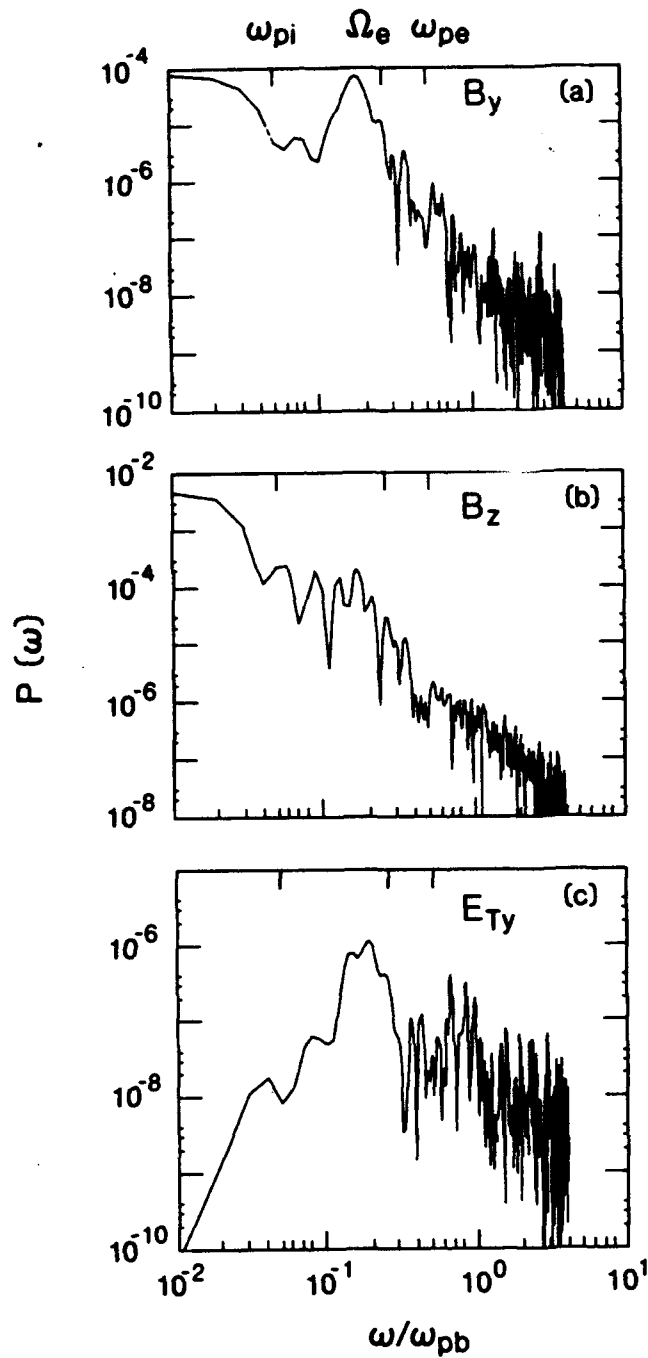


Figure 13. Power spectra for the  $B_y$ ,  $B_z$ , and  $E_{Ty}$  fields averaged over the interval  $0 < \omega_{pbt} < 200$  at a point  $\delta x/\Delta = 90$ ,  $\delta y/\Delta = 40$  away from the source of the electron beam. The ambient density is given by  $\Omega_e/\omega_{pe} = 0.5$ .

whistler waves propagating with a phase velocity of order  $c/10$ . The  $B_z$  spectrum shows a similar spectral intensity in the whistler region, but it produces only a shoulder on the much larger fields associated with the current sheet. The intense peaks at frequencies  $\lesssim \omega_{pi}$  are associated with the ion response to establish current closure across field lines. The total whistler wave energy is now about  $5 \times 10^{-5}$  of the electron beam energy injected up to time  $\omega_{pbt} = 80$ . This is now consistent with the Spacelab 2 observations. Similar results are obtained for a second simulation with  $\omega_{pe}/\Omega_e = 0.3$  except that the angles of propagation are somewhat larger, ranging from  $\approx 19^\circ$  down to  $\approx 8^\circ$  as a function of time.

With the present simulation parameters the spacecraft potential increases slowly with time (after a rapid initial jump and decay) and reaches a level of  $\approx 40\%$  of the beam energy by the end of the run ( $\omega_{pbt} = 200$ ). As a result of this charging, the ambient electron density is reduced on field lines connected to the spacecraft. This leads to the formation of a density depression extending out from the spacecraft whose spatial extent along the magnetic field increases with time at a speed of  $\approx v_p/3$ . The average density decrease is about a factor of two, but there are local depressions of a factor of four or more. The establishment of this density trough has a significant effect on the propagation of the whistler waves. For  $0.5 < \omega/\Omega_e < 1$ , whistler waves can be trapped in a density trough which then acts as a duct [see *e.g.*, *Smith et al.*, 1960]. This explains the observed decrease in propagation angle of the waves as a function of time as the trough expands. The density depressions produced in the simulations are considerably larger than the values of 2–10% necessary for trapping.

## 7. SPACECRAFT POTENTIAL CONTROL VIA INDIUM ION BEAM INJECTION

A recurring difficulty for space satellites making plasma observations concerns the accurate measurement of very cold plasma and/or low frequency electric fields during periods of high electrostatic surface potentials. Although scientific spacecraft have been equipped with conductive surfaces to eliminate differential charging between sunlit and shadowed surfaces, the fundamental problem of overall electrostatic charging remains. *Olsen* [1982] used the reduction of the spacecraft

potential during a transit from sunlight into eclipse for the identification of a cold plasma population previously undetected due to the masking effect of the positive surface potential.

The electrostatic potential of the spacecraft is a consequence of the current equilibrium between charged particles impacting on the surface and charges leaving the surface, such as photo-electrons, sputter-induced charged secondary particles, and artificially ejected charges [Pedersen *et al.*, 1987]. The extreme values of the electrostatic potential may range from less than -1000 Volts up to +1000 Volts [Garrett, 1981]. To maintain the spacecraft potential near the ambient plasma potential, an ion emission system that is small in size and resources is needed. A major constraint on such a system comes from the fact that its spacecraft resource requirements remain within a reasonable ratio with other instruments on the spacecraft and it should also be "quiet" in the sense of not interfering with other instruments onboard. Keeping these requirements in mind it was decided to develop new systems based on the use of liquid indium [Schmidt *et al.*, 1989].

Included in the instrumentation package for the upcoming Cluster and Geotail satellites will be a small compact ion emitter that contains a tiny amount of indium carried in a heater controlled containment device. Once the indium is heated to well above its melting point, the liquid metal flows due to surface tension along the shaft of a small needle. At its top the indium is ionized by field emission and emitted. The typical beam drift kinetic energy is 5 to 6 keV.

The main concern of the research we have carried out has been to examine whether the emitted indium ion beam can be unstable to electrostatic plasma instabilities for the various emitted beam and background conditions. For this study we restrict ourselves to a standard size spacecraft with conductive surfaces and to orbits outside the plasmasphere. Eclipse conditions are ignored and therefore the sunlit spacecraft will charge positive due to the dominance of sun-induced photo-electrons. The goal of the linear theory study is to identify any unstable wave modes that can occur such that effects that may result from these instabilities can be distinguished from other plasma physical processes. The detailed parameter search quantifies under what conditions the

indium ion beam can be emitted in such a way that an instability can be turned on or off during the mission.

## 8. OPERATING PRINCIPLES OF THE LIQUID METAL ION SOURCE (LMIS)

The ion emitter [Rüdenauer *et al.*, 1988] is a "solid-needle" type liquid metal ion source using indium as charged material [Dixon and von Engle, 1980]. Indium has an atomic number of 49 and its mass is 114.82. A tungsten needle with a tip radius of typically 2 to 15  $\mu$  is mounted in the indium reservoir which is attached to a heater. If the needle is well wetted by the metal, then the electrostatic stress at the needle's tip pulls the liquid indium towards the extractor electrode. This stress is counteracted by the surface tension. The resulting equilibrium is characterized by a stable field emission from a liquefied cone (Taylor cone) with a tip radius of 1 to 5 nm. The evaporation and resulting ionization leads to the emission of positively charged ions from the Taylor cone. Typical current densities at the cone apex are of the order of  $10^6 \text{cm}^{-2} \text{sr}^{-1} \text{A}$  for a beam energy of 10 keV. Ions leaving the surface are constantly replenished by hydrodynamic flow of liquid indium from the reservoir to the tip of the needle.

The typical operating characteristics of the LMIS require an extraction high voltage of 5 kV applied between extraction electrode and needle/reservoir. An emission current of 10  $\mu\text{A}$  requires a supply current of about 20  $\mu\text{A}$ , mostly due to focusing losses. The heater power required to maintain the indium reservoir well above the melting temperature is about 0.4 W. The beam divergence at the orifice is better than 15 (half-width), and the beam temperature  $\Delta E/E$  is better than  $10^{-3}$  at 1  $\mu\text{A}$ , with a weak dependence on the applied extraction voltage. The beam temperature depends on the emission current, which can be set by adjusting a current limiter inside the high voltage power supply. For small emission currents, around 1  $\mu\text{A}$ , the measured beam temperature is of the order of 40 eV. Increasing the emission current up to 10  $\mu\text{A}$  results in an increasing beam temperature (600 eV) that is mostly due to the appearance of a high energy tail.

For the linear theory study, we take the  $\text{In}^+$  beam drift energy to be 5 keV, which corresponds to a drift speed of about 91.3 km/s. The

temperature of the beam, as explained, is variable depending on the emission current setting and can range from 40 to 600 eV; the beam thermal speed will be a parameter that will be varied during the linear theory study.

## 9. LINEAR THEORY

A linear theory parameter search has been carried out to investigate whether particular combinations of ambient plasma parameters and emission modes of the indium ion beam exist such that electrostatic plasma instabilities may be excited. We consider a three species plasma with (1) an indium ion beam, (2) background electrons, and (3) background ions. The background plasma parameters vary depending on where the satellite is at the time of beam emission. For our study we considered four different background regions: the solar wind, the lobe, the plasma sheet boundary layer, and the central plasma sheet. Typical plasma parameters for each of these regions used in this study are found in Table 2, and are based on previous observations made in each region [*Frank, 1985; Lui, 1987; Rosenberg and Whipple, 1990*].

TABLE 2. Typical observed parameters for each of the four regions under consideration

Region	$T_i/T_e$	$\omega_{pe}/\Omega_e$	$T_e(\text{eV})$	$n_e(\text{cm}^{-3})$
CPS	5	5-20	> 1000	1
PSBL	2	5	~ 500	0.1
Lobe	2	1	< 100	0.01
Solar Wind	< 2	55-200	10	1-10

To understand the basic physics of unstable wave modes possible for this type of configuration, we first consider a cold plasma with magnetized electrons and unmagnetized ions. Following *Mikhailovskii [1975]*, the dispersion relation can be written as

$$0 = 1 - \frac{\omega_{pe}^2 \sin^2 \theta}{\omega^2 - \Omega_e^2} - \frac{\omega_{pe}^2 \cos^2 \theta}{\omega^2} - \frac{\omega_{pi}^2}{\omega^2} - \frac{\omega_{pb}^2}{(\omega - kU)^2} \quad (2)$$

where  $\omega_{pe}$ ,  $\omega_{pi}$ , and  $\omega_{pb}$  are the plasma frequencies of the background electrons, background ions and beam ions, respectively,  $\Omega_e$  is the electron gyrofrequency,  $\theta$  is the angle between the wavenumber  $\vec{k}$  and the external magnetic field, and  $\vec{U}$  is the inidum beam drift velocity. We assume that  $\vec{k}$  and  $\vec{U}$  are aligned. The frequency  $\omega$  is complex with  $\omega = \omega_r + i\gamma$ .

An unstable interaction between the beam mode and the lower hybrid mode occurs at very oblique wave propagation ( $\theta \sim 90^\circ$ ) when  $\omega_r = \omega_{lh} \approx kU$ , where the lower hybrid frequency is given by

$$\omega_{lh} = \frac{\omega_{pi}}{\sqrt{1 + \omega_{pe}^2/\Omega_e^2}} \quad (3)$$

in the limit of unmagnetized ions, i.e.,  $\omega_{pi} \gg \Omega_i$ . The growth rate for this instability is given by

$$\gamma \approx \frac{\omega_{lh} \alpha^{1/3}}{[1 + (m_i/m_e) \cos^2 \theta]^{1/3}} \quad (4)$$

where  $\alpha = n_b m_i / n_i m_b \ll 1$ ,  $n_b$  and  $m_b$  are the beam density and mass,  $n_i$  and  $m_i$  are the background ion density and mass, and  $m_e$  is the background electron mass. The wave growth is due to a fluid-type instability driven by the net drift between the beam and background plasma, and it is interesting to note from equation (4) that the growth rate maximizes when  $\theta = 90^\circ$ .

If we consider the case where the inidum beam is not strictly cold, but is approximated by a Maxwellian velocity distribution, a beam driven lower hybrid instability with real frequency given by equation (3) is still present, but the growth rate is modified and can be expressed as

$$\gamma = \left( \frac{U}{v_{tb}} \right)^2 \frac{\alpha \omega_{lh}}{1 + (m_i/m_e) \cos^2 \theta} \quad (5)$$

where  $v_{tb}$  is the beam thermal speed. As in the cold plasma case, the instability maximizes for transverse wave propagation ( $\theta = 90^\circ$ ), but for a warm beam the growth rate is sensitive to the beam drift to thermal speed ratio  $U/v_{tb}$ , such that as the beam temperature increases for a given drift speed, the growth rate will decrease.

To study the parametric dependence of this instability for the different background regions and beam emission modes, we have solved the fully magnetized warm electrostatic dispersion relation numerically. The form for the general electrostatic dispersion relation can be found in *Harris* [1959] or *Stix* [1962]. An example of the dispersion relation for the indium ion beam ejected while the satellite is in the plasma sheet boundary layer is shown in Figure 14. The beam drift speed to thermal speed ratio used for this figure is  $U/v_{tb} = 17$  and the beam density is  $n_b/n_e = 0.5$ . Plotted is frequency versus wavenumber with the real frequency shown by the solid line and the growth rate shown by the dashed line. In Figure 14, the wave propagation angle is varied and the results confirm that found from equations (4) and (5), whereby the growth rate maximizes for purely transverse wave propagation ( $\theta = 90^\circ$ ). Keep in mind that the beam is directed parallel to  $\vec{k}$ , which means that maximum wave growth occurs for the beam being emitted  $90^\circ$  to the external magnetic field. The real frequency at maximum wave growth is less than the lower hybrid frequency given in equation (3), due to warm plasma effects of the background ions.

Now maintaining transverse wave propagation ( $\theta = 90^\circ$ ) to find maximum wave growth, we plot in Figures 15, 16, 17, and 18 the dispersion relation for beam emission in the central plasma sheet, plasma sheet boundary layer, solar wind, and lobe, respectively (the background parameters are listed in Table 2). The format for these figures is the same as in Figure 14, and the beam density is the same; however, the ratio  $U/v_{tb}$  is varied (keeping  $U$  fixed corresponding to a beam drift energy of 5 keV) for each region to find the instability threshold. As expected from equation (5) the growth rate decreases as  $U/v_{tb}$  decreases, which corresponds to an increase in the beam temperature. From Figures 15 through 18 it can be seen that the central plasma sheet has the lowest threshold for the beam instability as a function of beam temperature, which means that the indium beam can be fairly warm and still drive an instability there. The lobe, on the other hand, has the highest threshold whereby the beam must be relatively cool (low emission current) for an instability to exist.

### Plasma Sheet Boundary Layer Dispersion Relation

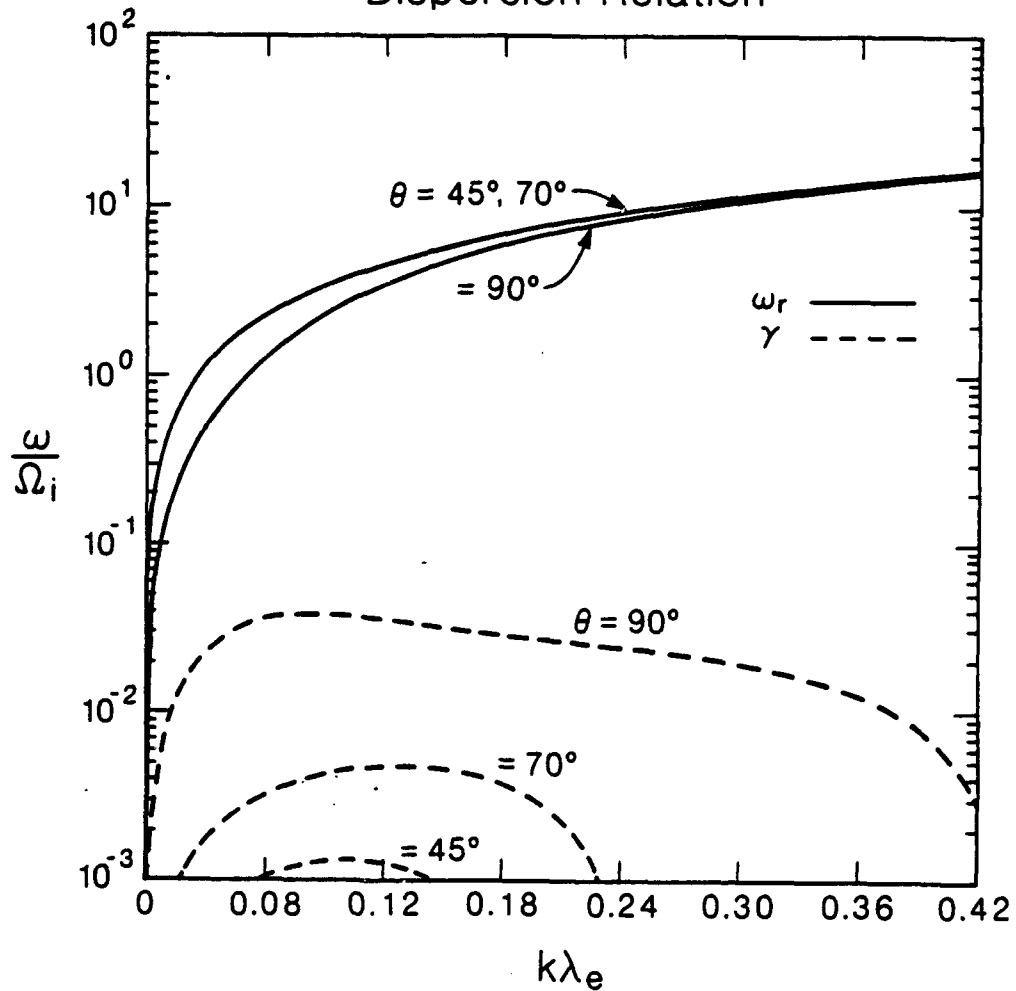


Figure 14. This figure shows the dispersion of low frequency waves found from numerical solutions of the general warm plasma dispersion relation for an indium ion beam emitted while the satellite is in the plasma sheet boundary layer. Plotted is frequency (normalized to the background ion gyrofrequency) versus wavenumber (times the electron Debye length). The solid line corresponds to the real frequency and the growth rates are shown by the dashed line for three different wave propagation angles. Note the growth rate maximizes for transverse wave propagation.

## Central Plasma Sheet Dispersion Relation

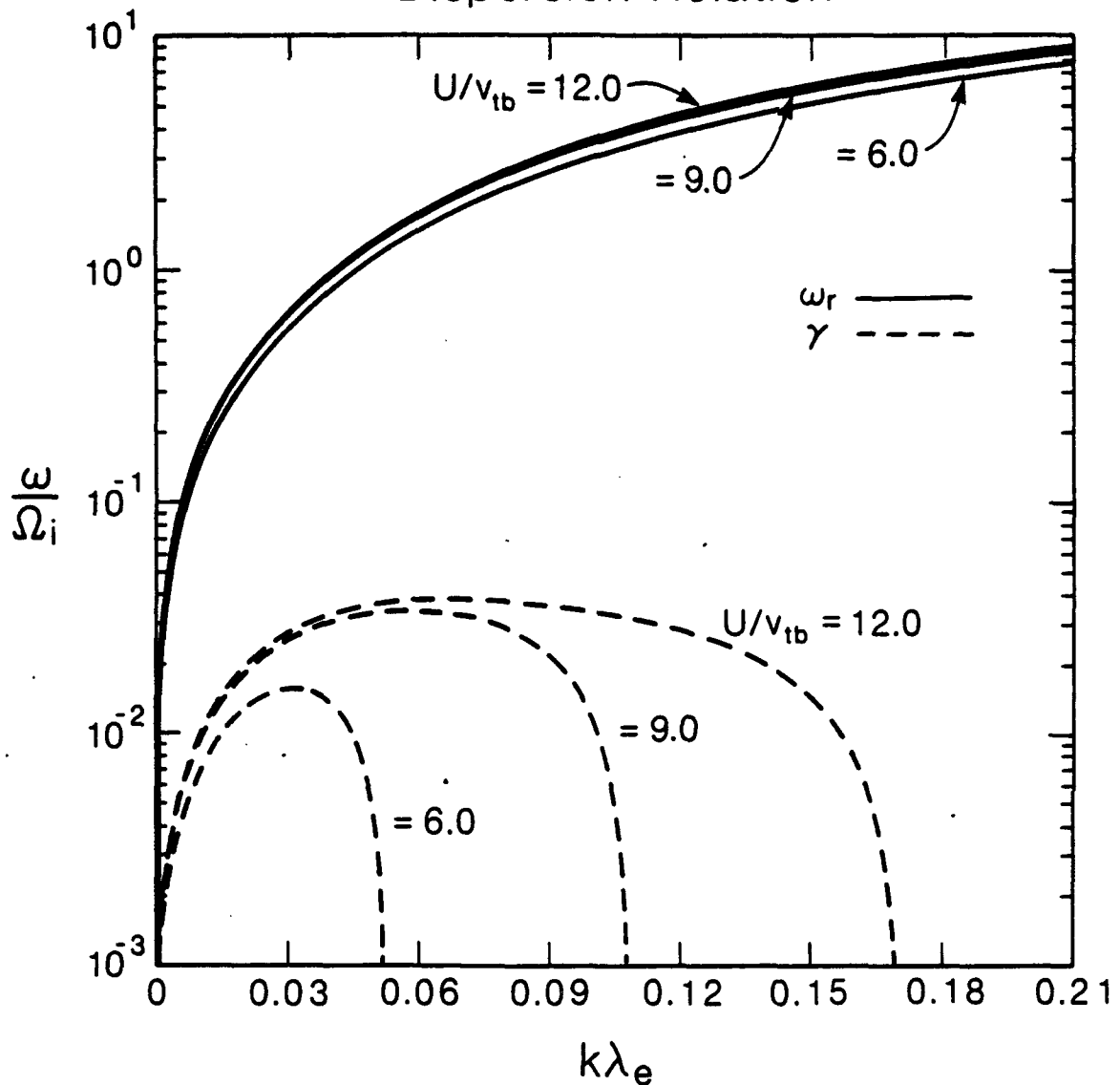


Figure 15. The wave dispersion relation when the indium beam is emitted in the central plasma sheet. The format is the same as Figure 14, but here the ratio  $U/v_{tb}$  is varied and the lowest value where there is still an appreciable instability is shown. The background plasma parameters are found in Table 2. In this case, if  $U/v_{tb}$  falls below 6, no instability is possible.

## Plasma Sheet Boundary Layer Dispersion Relation

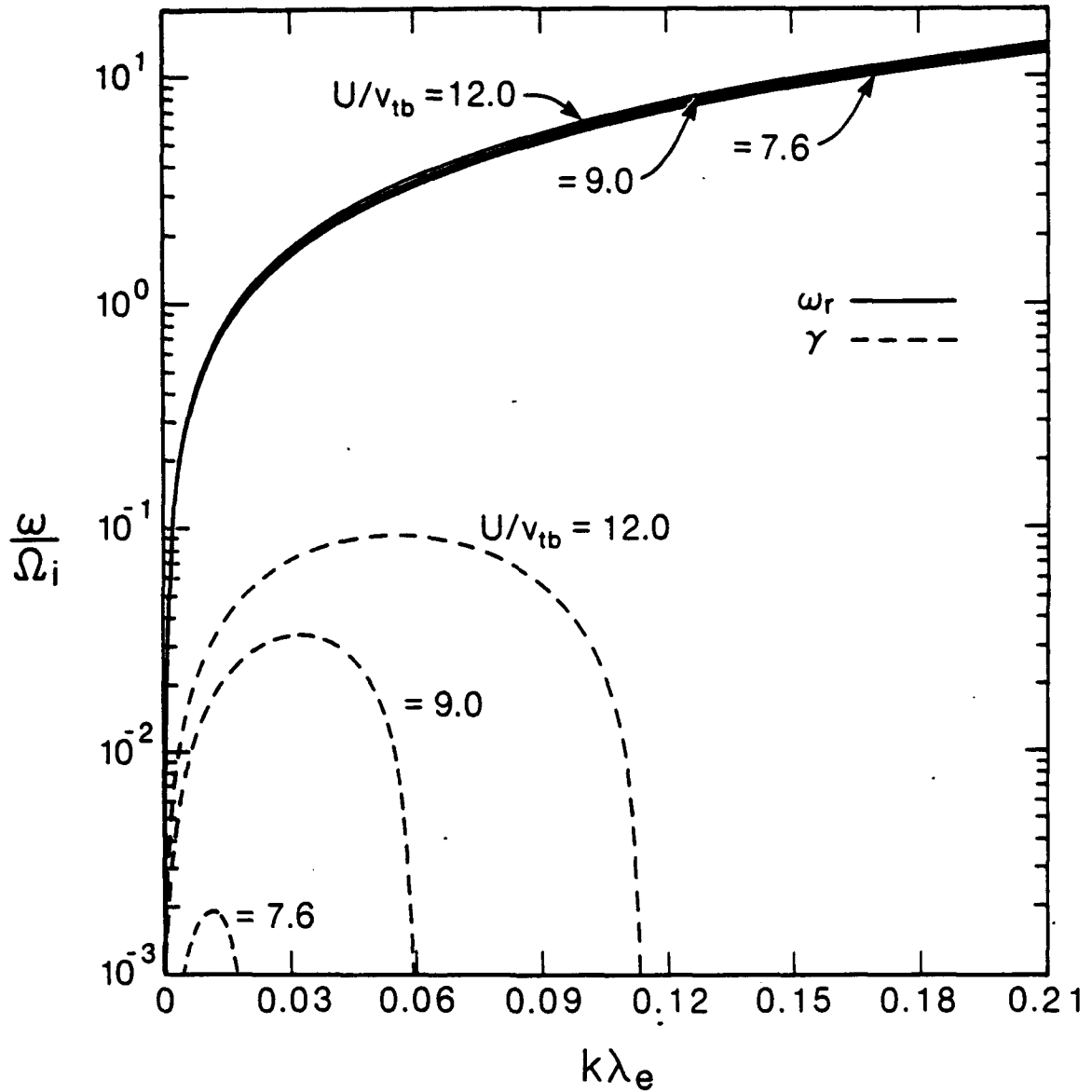


Figure 16. Dispersion relation for beam emission in the plasma sheet boundary layer. The format is the same as in Figure 15, with the background parameters found from Table 2.

## Solar Wind Dispersion Relation

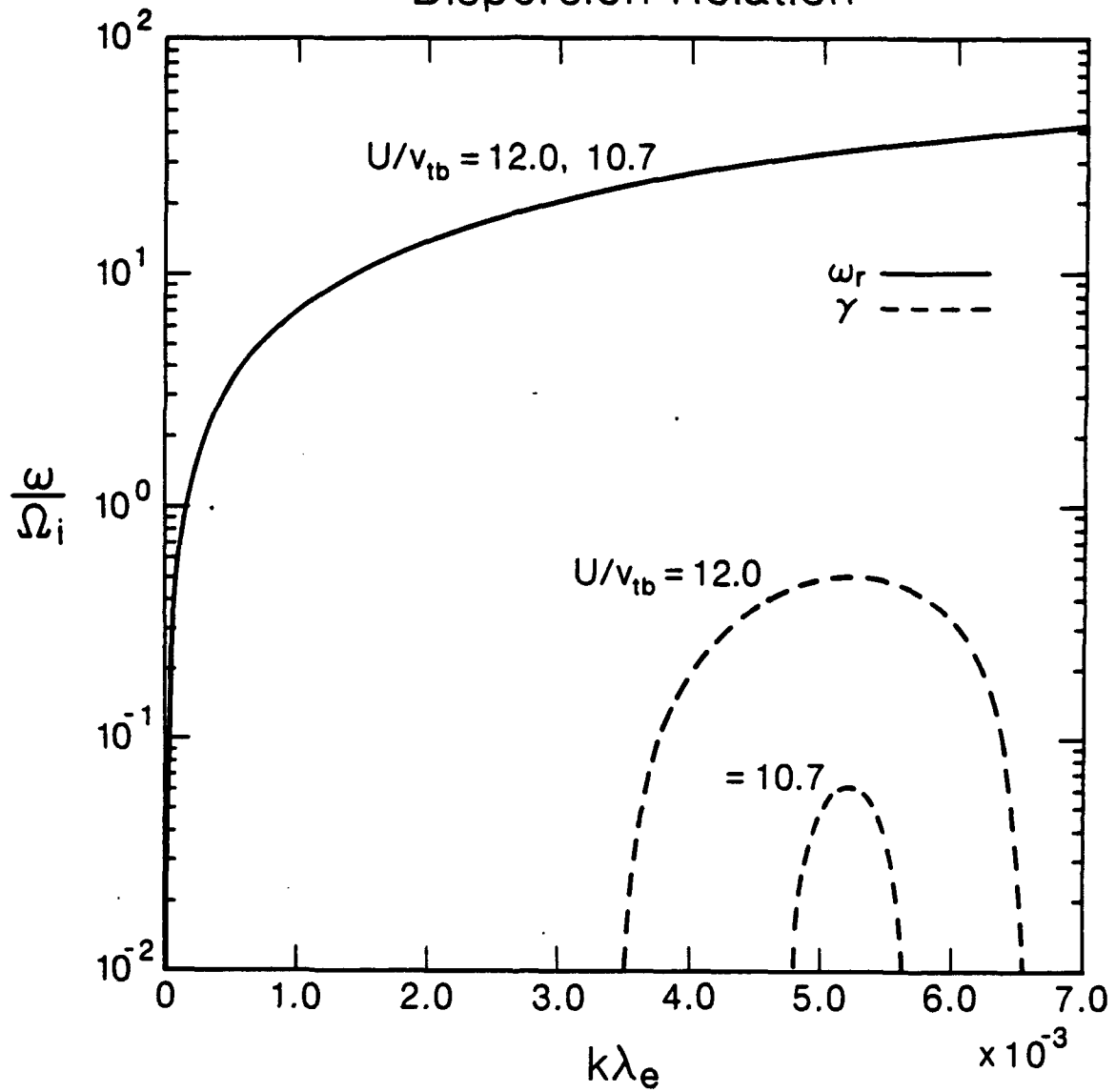


Figure 17. Dispersion relation for beam emission in the solar wind. The format is the same as in Figure 15, with the background parameters found from Table 2.

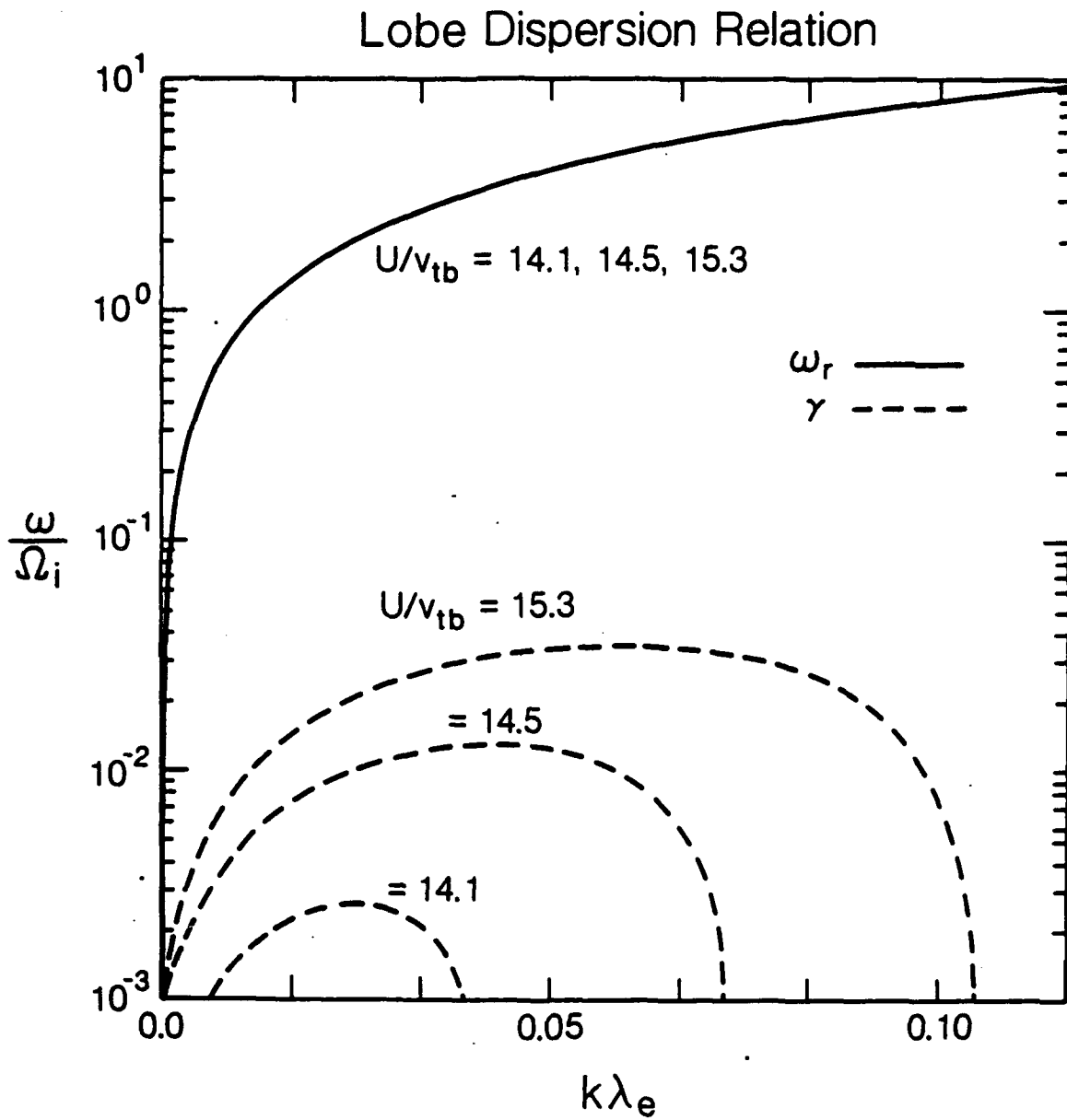


Figure 18. Dispersion relation for beam emission in the lobe. The format is the same as in Figure 15, with the background parameters found from Table 2. Note that this region has the highest threshold for instability compared to the others.

## 10. SUMMARY

An indium ion beam device will be placed on future satellites such as Geotail and Cluster to control the spacecraft potential. A study has been carried out to see if the emitted indium ion beam can be unstable when the satellite is in various regions of the Earth's magnetosphere and solar wind. Linear theory for electrostatic waves shows that an ion beam driven lower hybrid instability can be excited with maximum growth at wave propagation (and beam emission) transverse to the external magnetic field.

Numerical results from the linear theory parameter search show that for the expected indium beam conditions and typical parameters for the background plasma that the central plasma sheet will have the lowest threshold for instability, while the lobe will have the highest. Since the emission current, which controls the beam thermal speed, can be varied during the satellite mission, the linear theory results can be tested directly by changing the current and using observed wave data to see whether an instability in the right frequency range is excited and turns on or off according to the stability criteria. Also, depending on the orientation of the beam emitter with the external magnetic field, the linear theory conclusion that maximum wave growth will occur for transverse emission can be tested.

## REFERENCES

- Banks, P.M., and W.J. Raitt, Observations of electron beam structure in space experiments, *J. Geophys. Res.*, **93**, 5811 (1988).
- Dawson, J.M., and R. Shanny, Some investigations of nonlinear behavior in one-dimensional plasmas, *Phys. Fluids*, **11**, 1506 (1968).
- Dixon, A.J., and A. vonEngle, Studies of field emission gallium ion sources, *Inst. Conf. Ser.*, **54**, 292 (1980).
- Farrell, W.M., D.A. Gurnett, P.M. Banks, R.I. Bush, and W.J. Raitt, An analysis of whistler mode radiation from the Spacelab 2 electron beam, *J. Geophys. Res.*, **93**, 153 (1988).
- Frank, L.A., Plasmas in the earth's magnetotail, *Space Sci. Rev.*, **42**, 211 (1985).
- Garrett, H.B., The charging of spacecraft surfaces, *Rev. Geophys. Space Sci.*, **19**, 744 (1981).
- Gurnett, D.A., W.S. Kurth, J.T. Steinberg, P.M. Banks, R.I. Bush and W.J. Raitt, Whistler-mode radiation from the Spacelab 2 electron beam, *Geophys. Res. Lett.*, **13**, 225 (1986).
- Harris, E.G., Unstable plasma oscillations in a magnetic field, *Phys. Rev. Lett.*, **2**, 34 (1959).
- Hess, W.N., M.C. Trichel, T.N. Davis, W.C. Beggs, G.E. Kraft, E. Stassinopoulos, and E.J. R. Maier, Artificial auroral experiment: Experiment and principal results, *J. Geophys. Res.*, **76**, 6067 (1971).
- Hockney, R.W., Formation and stability of virtual electrodes in a cylinder, *J. Appl. Phys.* **38**, 4166 (1968).
- Junginger, H., G. Geiger, G. Haerendel, F. Melzner, E. Amata, and B. Higel, A statistical study of dayside magnetospheric electric field fluctuations with periods between 150 and 600 s, *J. Geophys. Res.*, **89**, 5495 (1984).
- Katz, I., G.A. Jongeward, D.E. Parks, D.L. Reasoner, and C.K. Purvis, Energy broadening due to space-charge oscillations in high current electron beams, *Geophys. Res. Lett.*, **13**, 64 (1986).
- Lui, A.T.Y., Road map to magnetotail dynamics, *Magnetotail Physics*, edited by A.T.Y. Lui, p. 1, Johns Hopkins University Press, Baltimore, MD (1987).

- Maelhlum, B.M., J. Troim, N.C. Maynard, W.F. Denig, M. Friedrich, and K.M. Torkar, Studies of the electrical charging of the tethered electron accelerator mother-daughter rocket MAIMIK, *Geophys. Res. Lett.*, *15*, 725 (1988).
- Mansfield, V.N., Radiation from a charged particle spiraling in a cold magnetoplasma, *Astrophys. J.*, *147*, 672 (1967).
- Melzner, F., G. Metzner, and D. Antrack, The GEOS electron beam experiment S329, *Space Sci. Instrum.*, *4*, 45 (1978).
- Mikhailovskii, A.B., *Theory of Plasma Instabilities*, McGraw Hill, New York, NY (1975).
- Myers, N.B., W.J. Raitt, B.E. Gilchrist, P.M. Banks, T. Neubert, P.R. Williamson, and S. Sasaki, A comparison of current-voltage relationships of collectors in the Earth's ionosphere with and without electron beam emission, *Geophys. Res. Lett.*, *16*, 365 (1989).
- Neubert, T., and P.M. Banks, Recent results from studies of electron beam phenomena in space plasmas, *Planet. Space Sci.*, *40*, 153 (1992).
- Obayashi, T., N. Kawashima, S. Sasaki, M. Yanagisawa, K. Kuriki, M. Nagatomo, K. Ninomiya, W.T. Roberts, W.W.L. Taylor, P.R. Williamson, P. Banks, D.L. Reasoner and J.L. Burch, Initial results of SEPAC scientific achievements, *Earth Oriented Appl. Space Technol.*, *5*, 37 (1985).
- Okuda, H., R. Horton, M. Ono, and M. Ashour-Abdalla, Propagation of a nonrelativistic electron beam in a plasma in a magnetic field, *Phys. Fluids*, *30*, 200 (1987).
- Olsen, R.C., The hidden ion population of the magnetosphere, *J. Geophys. Res.*, *87*, 3481 (1982).
- Pedersen, A., C.A. Cattell, C.G. Fälthammar, V. Formisano, P.A. Lindqvist, F. Mozer, and R. Torbert, Quasi-static electric field measurements with spherical double probes on the GEOS and ISEE satellites, *Space Sci. Rev.*, *37*, 269 (1987).
- Pritchett, P.L., Spatial coherence during pulsed injection of electron beams, *J. Geophys. Res.*, *95*, 10,671 (1990).
- Pritchett, P.L., A three-dimensional simulation model for electron beam injection experiments in space, *J. Geophys. Res.*, *96*, 13,781 (1991).

- Pritchett, P.L., and R.M. Winglee, The plasma environment during particle beam injection into space plasmas: 1. Electron beams, *J. Geophys. Res.*, **92**, 7673 (1987).
- Pritchett, P.L., H. Karimabadi, and N. Omidi, Generation mechanism of whistler waves produced by electron beam injection in space, *Geophys. Res. Lett.*, **16**, 883 (1989).
- Rosenberg, M., and E. Whipple, Propagation and beam-plasma interactions of the EDI beam, *Proceedings of the AIAA 21st Fluid Dynamics, Plasma Dynamics and Lasers Conference, AIAA 90-1567*, 1 (1990).
- Rüdenauer, F.G., W. Steiger, H. Arends, M. Fehringer, and R. Schmidt, A liquid metal ion source for space application, *J. de Physique*, **49**, 161 (1988).
- Sasaki, S., K.-I. Oyama, N. Kawashima, W.J. Raitt, and N.B. Myers, VLF and HF wave characteristics observed from an active experiment tethered mother/daughter rocket payload (CHARGE-2), *EOS*, **67**, 1170 (1986).
- Schmidt, R., H. Arends, K. Torkar, and N. Valavanoglou, Novel methods for active spacecraft potential control, *AGU Geophysical Monograph* (1989).
- Smith, R.L., R.A. Helliwell, and I.W. Yabroff, A theory of trapping of whistlers in field-aligned columns of enhanced ionization, *J. Geophys. Res.*, **65**, 815 (1960).
- Stix, T.H., *Theory of Plasma Waves*, McGraw-Hill, New York, NY (1962).
- Winckler, J.R., The application of artificial electron beams to magnetospheric research, *Rev. Geophys.*, **18**, 659, (1980).
- Winckler, J.R., Artificial electron beams in the magnetosphere and ionosphere, in *Physics of Space Plasmas (1989)*, *SPI Conference Proceedings and Reprint Series*, Number 9, T. Chang, G.B. Crew, and J.R. Jasperse, eds. (Scientific Publishers, Inc., Cambridge, MA, 1990), p. 385.
- Winckler, J.R., P.R. Malcolm, R.L. Arnoldy, W.J. Burke, K.N. Erickson, J. Ernstmeyer, R.C. Franz, T.J. Hallinan, P.J. Kellogg, S.J. Monson, K.A. Lynch, G. Murphy, and R.J. Nemzek, ECHO 7: An electron beam experiment in the magnetosphere, *EOS, Trans. AGU*, **70**, 657 (1989).

- Winglee, R.M., Electron beam injection during active experiments. 2, Collisional effects, *J. Geophys. Res.*, 95, 6191 (1990).
- Winglee, R.M., and P.L. Pritchett, Space-charge effects during the injection of dense electron beams into space plasma, *J. Geophys. Res.*, 92, 6114, (1987).
- Winglee, R.M., and P.L. Pritchett, Comparative study of cross-field and field-aligned electron beams in active experiments, *J. Geophys. Res.*, 93, 5823 (1988).